

BRAIxDet: Learning to Detect Malignant Breast Lesion with Incomplete Annotations

Yuanhong Chen^a, Yuyuan Liu^a, Chong Wang^{a,*}, Michael Elliott^b, Chun Fung Kwok^b, Carlos Peña-Solorzano^b, Yu Tian^a, Fengbei Liu^a, Helen Frazer^c, Davis J. McCarthy^{b,d}, Gustavo Carneiro^a

^aAustralian Institute for Machine Learning, The University of Adelaide, Adelaide, Australia

^bBioinformatics and Cellular Genomics, St Vincent's Institute of Medical Research, Melbourne, Australia

^cSt Vincent's Hospital Melbourne, Melbourne, Australia

^dMelbourne Integrative Genomics, The University of Melbourne, Melbourne, Australia

ARTICLE INFO

Article history:

Received 1 May 2013

Received in final form 10 May 2013

Accepted 13 May 2013

Available online 15 May 2013

Keywords:

Deep learning

Multi-view learning

Breast cancer screening

Incomplete annotations

Malignant lesion detection

Student-teacher Learning

ABSTRACT

Methods to detect malignant lesions from screening mammograms are usually trained with fully annotated datasets, where images are labelled with the localisation and classification of cancerous lesions. However, real-world screening mammogram datasets commonly have a subset that is fully annotated and another subset that is weakly annotated with just the global classification (i.e., without lesion localisation). Given the large size of such datasets, researchers usually face a dilemma with the weakly annotated subset: to not use it or to fully annotate it. The first option will reduce detection accuracy because it does not use the whole dataset, and the second option is too expensive given that the annotation needs to be done by expert radiologists. In this paper, we propose a middle-ground solution for the dilemma, which is to formulate the training as a weakly- and semi-supervised learning problem that we refer to as malignant breast lesion detection with incomplete annotations. To address this problem, our new method comprises two stages, namely: 1) pre-training a multi-view mammogram classifier with weak supervision from the whole dataset, and 2) extending the trained classifier to become a multi-view detector that is trained with semi-supervised student-teacher learning, where the training set contains fully and weakly-annotated mammograms. We provide extensive detection results on two real-world screening mammogram datasets containing incomplete annotations and show that our proposed approach achieves state-of-the-art results in the detection of malignant breast lesions with incomplete annotations.

© 2024 Elsevier B. V. All rights reserved.

1. Introduction

Breast cancer is the most commonly diagnosed cancer worldwide and the leading cause of cancer-related death in women (Sung et al., 2021). One of the most effective ways to increase the survival rate relies on the early detection of breast cancer (Lauby-Secretan et al., 2015) using screening mammograms (Selvi, 2014). The analysis of screening mammograms is generally done manually by radiologists, with the eventual help of Computer-Aided Diagnosis (CAD) tools to assist with the detection and classification of breast lesions (Hadjjiiski et al., 2006; Shen et al., 2019a). However, CAD tools have shown inconsistent results in clinical settings. Some research groups (Brem et al., 2003; Hupse and Karssemeijer, 2009; Hupse et al., 2013) have shown promising results, where

radiologists benefited from the use of CAD systems with an improved detection sensitivity. However, other studies (Lehman et al., 2015; Fenton et al., 2007, 2011) do not support the reimbursement of the costs associated with the use of CAD systems, estimated to be around \$400 million a year (Lehman et al., 2015), since experimental results show no benefits in terms of detection rate.

The use of deep learning (LeCun et al., 2015) for the analysis of screening mammograms is a promising approach to improve the accuracy of CAD tools, given its outstanding performance in other learning tasks (He et al., 2016; Ren et al., 2015). For example, Shen et al. (2019b, 2021) proposed a classifier that relies on concatenated features from a global network (using the whole image) and a local network (using image patches). To leverage the cross-view information of mammograms, Carneiro et al. (2017) explored different feature fusion strategies to integrate the knowledge from multiple mammographic views to enhance classification performance. However, these studies that focus on classification without producing reliable lesion de-

*Corresponding author.

e-mail: chong.wang@adelaide.edu.au (Chong Wang)

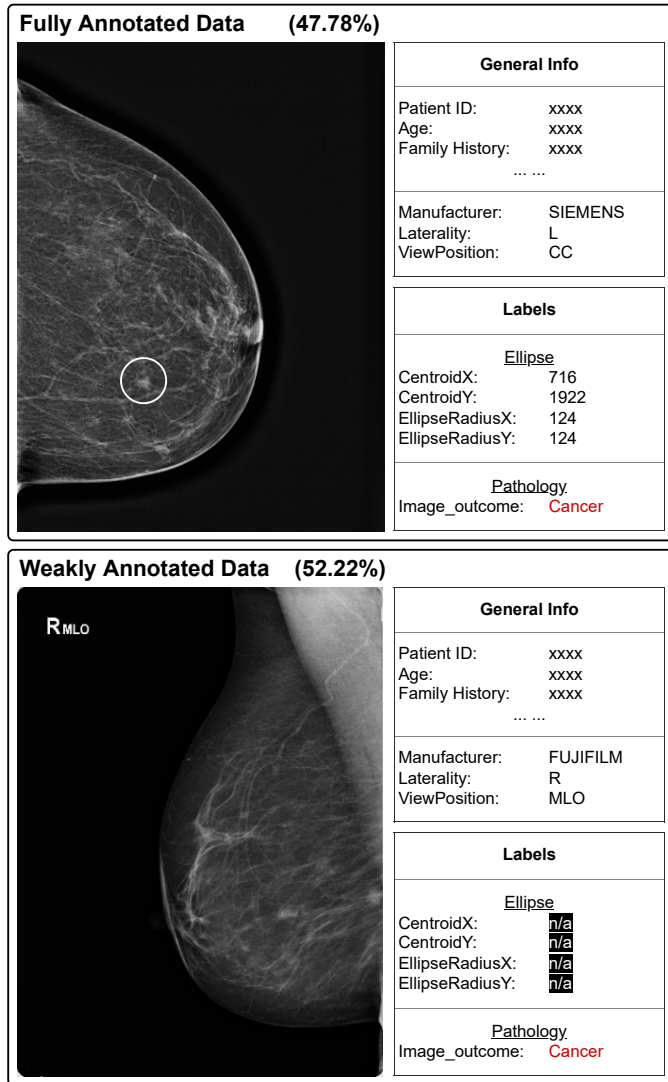


Fig. 1. The data structure of our ADMANI dataset, showing fully (top, representing 47.78% of the data) and weakly (bottom, representing the remaining 52.22% of the data) annotated mammograms.

tection results may not be useful in clinical practice. Lesion detection from mammograms has been studied by Ribli et al. (2018) and Dhungel et al. (2015), who developed CAD systems based on modern visual object detection methods. Ma et al. (2021) implemented a relation network (Hu et al., 2018) to learn the inter-relationships between the region proposals from ipsi-lateral mammographic views. Yang et al. (2020, 2021) proposed a system that focused on the detection and classification of masses from mammograms by exploring complementary information from ipsilateral and bilateral mammographic views.

Although the mammographic lesion detection methods above show encouraging performance, they are trained on fully annotated datasets, where images are labelled with the classification and localisation of cancerous lesions. Such setup is uncommon in large-scale real-world screening mammogram datasets that usually have a subset of the images annotated with classification and localisation of lesions, and the other subset annotated with

only the global classification. For example, our own Annotated Digital Mammograms and Associated Non-Image (ADMANI) dataset, which has been collected from the BreastScreen Victoria (Australia) population screening program, has a total of 4,084,098 images, where only 47.78% of the 21,399 cancer cases are annotated with classification and localisation of lesions, and the rest 52.22% of the cases are weakly annotated, as displayed in Figure 1. Given the large size of such datasets, it is rather disadvantageous not to use these weakly annotated images for training, but at the same time, it is too expensive to have them annotated by radiologists. Therefore, in this paper we propose a middle-ground solution, which is to formulate the training as a weakly- and semi-supervised learning problem that is referred to as malignant breast lesion detection with incomplete annotations.

To address the incomplete annotations learning problem described above, we introduce a novel multi-view lesion detection method, called BRAIxDet. BRAIxDet is trained using a two-stage learning strategy that utilises all training samples from the dataset. In the first stage, we pre-train our previously proposed multi-view classification network BRAIxMVCCL (Chen et al., 2022) on the whole weakly-supervised training set, where images are annotated only with their global labels.

This pre-training enables BRAIxMVCCL to produce a strong feature extractor and a post-hoc explanation based on Grad-CAM (Selvaraju et al., 2017). In the second stage, we transform BRAIxMVCCL into the detector BRAIxDet which is trained using a student-teacher semi-supervised learning mechanism. More specifically, the student is trained from fully- and weakly-supervised subsets, where the weakly-supervised images have their lesions pseudo-labelled by the teacher’s detections and BRAIxMVCCL’s Grad-CAM results. Furthermore, the teacher is trained from the exponential moving average (EMA) of the student’s parameters, where the batch normalization (BN) statistic used in the EMA is frozen after pre-training to alleviate the issues related to the dependency on the samples used to train the student, and the mismatch of model parameters between student and teacher. The major contributions of this paper are summarised as follows:

- We explore a **new experimental setting for the detection of malignant breast lesions** using large-scale real-world screening mammogram datasets that have incomplete annotations, with a subset of images annotated with the classification and localisation of lesions and a subset of images annotated only with image classification, thus forming a weakly- and semi-supervised learning problem.
- We propose a **new two-stage training method to handle the incomplete annotations** introduced above. The first stage uses the images annotated with their classification labels to enable a weakly-supervised pre-training of our previously proposed multi-view classification model BRAIxMVCCL (Chen et al., 2022). The second stage transforms the multi-view classifier BRAIxMVCCL into the detector BRAIxDet, which is trained with a student-teacher semi-supervised learning approach that uses both the weakly- and the fully-supervised subsets.

- We also propose innovations to the student-teacher semi-supervised detection learning, where the student is trained using the teacher’s detections and BRAIxMVCCL’s Grad-CAM (Selvaraju et al., 2017) outputs to estimate lesion localisation for the weakly-labelled data; while the teacher is trained with the temporal ensembling of student’s parameters provided by EMA, with the BN parameters frozen after pre-training to mitigate the problems introduced by the dependency on the student training samples, and the mismatch between student and teacher model parameters.
- We provide extensive experiments on two real-world breast cancer screening mammogram datasets containing incomplete annotations.

Our proposed BRAIxDet model achieves state-of-the-art (SOTA) performance on both datasets in terms of lesion detection measures.

2. Related work

2.1. Lesion detection in mammograms

Object detection is a fundamental task in computer vision (Liu et al., 2020a). The existing detection methods can be categorized into two groups: 1) two-stage methods (Girshick, 2015; Ren et al., 2015) that first generate region proposals based on local objectiveness, and then classify and refine the detection of these region proposals; and 2) single-stage methods (Redmon et al., 2016; Carion et al., 2020) that directly output bounding box predictions and corresponding labels. In general, the two-stage methods are preferred for non-real-time medical image analysis applications, such as lesion detection from mammograms (Ma et al., 2021; Yang et al., 2020, 2021), since they usually provide more accurate detection performance. On the other hand, single-stage methods tend to be less accurate but faster, which is more suitable for real-time applications, such as assisted intervention (Butler et al., 2022). Similar to previous papers that propose lesion detection methods from mammograms (Ma et al., 2021; Yang et al., 2020, 2021), we adopt the two-stage method Faster-RCNN (Ren et al., 2015) as our backbone detector since the detection accuracy is more important than speed in our clinical setting.

A standard screening mammogram exam contains two ipsilateral projection views of each breast, namely bilateral cranio-caudal (CC) and mediolateral oblique (MLO), where radiologists analyse both views simultaneously by searching for global architectural distortions and local cancerous lesions (e.g., masses and calcifications). Recently, fully-supervised learning methods (i.e., methods containing training sets with complete lesion localisation and classification annotations) have shown promising results for mass detection from single-view (Ribli et al., 2018; Dhungel et al., 2015) and multi-view mammograms (Ma et al., 2021; Liu et al., 2020b; Yang et al., 2020, 2021). However, these methods only focus on the detection and classification of masses (i.e., not all cancerous lesions), limiting their scope and application. Similarly to previous multi-view mammogram analysis methods (Ma et al., 2021; Liu et al., 2020b; Yang et al., 2020, 2021), BRAIxMVCCL

is designed to learn complementary information from ipsilateral mammogram views (CC and MLO). Unlike previous methods that depend on the ill-defined registration between the two views (e.g., based on nipple alignment (Yang et al., 2020, 2021), or geometric features (Ma et al., 2021; Liu et al., 2019)), BRAIxMVCCL realises multi-view information integration via implicit reasoning with a local co-occurrence module. Also, BRAIxMVCCL explicitly considers the global consistency between ipsilateral views to enhance the representation ability. Furthermore, BRAIxMVCCL is trained with an end-to-end learning method that is simpler and more efficient than the multi-stage learning algorithms to train other multi-view approaches (Yang et al., 2020, 2021). Nevertheless, real-world screening mammogram datasets tend not to exclusively contain fully annotated images – instead, these datasets usually have a subset that is annotated with lesion localisation and classification, and another subset that is weakly annotated only with the global image classification labels. Instead of discarding the weakly annotated images or hiring a radiologist to annotate these images, we propose a new weakly- and semi-supervised learning approach that can use both subsets of the dataset, without adding new detection labels.

2.2. Weakly-supervised object detection

Weakly supervised disease localisation (WSDL) is a challenging learning problem that consists of training a model to localise a disease in a medical image, even though the training set contains only global image classification labels without any disease localisation labels. WSDL approaches can be categorized into class activation map (CAM) methods (Zhou et al., 2016), multiple instance learning (MIL) methods (Oquab et al., 2015), and prototype-based methods (Chen et al., 2019).

CAM methods leverage the gradients of the target disease at the last convolution layer of the classifier to produce a coarse heatmap. This heatmap highlights areas that contribute most to the classification of the disease in a post-hoc manner. For example, Rajpurkar et al. (2017) adopted GradCAM (Selvaraju et al., 2017) to achieve WSDL in chest X-rays. Lei et al. (2020) extended the original CAM (Zhou et al., 2016) to learn the importance of individual feature maps at the last convolution layer to capture fine-grained lung nodule shape and margin for lung nodule classification. **MIL-based methods** regard each image as a bag of instances and encourage the prediction score for positive bags to be larger than for the negative ones. To extract region proposals included in each bag, early methods (Oquab et al., 2015) adopted max pooling to concentrate on the most discriminative regions. To avoid the selection of imprecise region proposals, Noisy-OR (Wang et al., 2017), softmax (Seibold et al., 2020), and Log-Sum-Exp (Wang et al., 2017; Yao et al., 2018) pooling methods have been used to maintain the relative importance between instance-level predictions and encourage more instances to affect the bag-level loss. **Prototype-based methods** aim to learn class-specific prototypes, represented by learned local features associated with each class, where classification and detection are achieved by assessing the similarity between image and prototype features, producing a detection map per prototype (Chen et al., 2019). The major

weakness of WSDL methods is that they are trained only with image-level labels, so the model can only focus on the most discriminative features of the image, which generally produce too many false positive lesion detections.

2.3. Semi-supervised object detection

Large-scale real-world screening mammogram datasets usually contain a subset of fully-annotated images, where all lesions have localisation and classification labels, and another subset of images with incomplete annotations represented by the global classification labels. Such setting forms a semi-supervised learning (SSL) problem, where part of the training does not have the localisation label. There are two typical SSL strategies, namely: pseudo-label methods (Sohn et al., 2020; Liu et al., 2021; Xu et al., 2021) and consistency learning methods (Jeong et al., 2019).

Pseudo-label methods are usually explored in a student-teacher framework, where the main idea is to train the teacher network with the fully-annotated subset, followed by a training of the student model with pseudo-labels produced by the teacher for the unlabelled data. Sohn et al. (2020) proposed STAC, a detection model pre-trained using labelled data and used to generate labels for unlabelled data, which is then used to fine-tune the model. The unbiased teacher method (Liu et al., 2021) generates the pseudo-labels for the student, and the student trains the teacher with EMA (Tarvainen and Valpola, 2017), where the teacher and student use different augmented images, and the foreground and background imbalances are dealt with the focal loss (Lin et al., 2017). Soft teacher (Xu et al., 2021) is based on an end-to-end learning paradigm that gradually improves the pseudo-label accuracy during the training by selecting reliable predictions. The pseudo-labelling methods above have the advantage of being straightforward to implement for the detection problem. However, when fully-annotated data is scarce, the student network can overfit the incorrect pseudo-labels, which is a problem known as confirmation bias that leads to poor model performance.

Consistency learning methods train a model by minimizing the difference between the predictions produced before and after applying different types of perturbations to the unlabelled images. Such strategy is challenging to implement for object detection because of the difficulty to accurately match the detected regions across various locations and sizes after perturbation. Recently proposed methods (Jeong et al., 2019; Xu et al., 2021) use one-to-one correspondence perturbation (such as cutout and flipping) to solve this problem. Nevertheless, such strong perturbations are not suitable for medical image detection since they could erase malignant lesions. Also, perturbations applied to pixel values (e.g., color jitter) are not helpful for mammograms since they are grey-scale images. Furthermore, searching for the optimal combination of the perturbations and the hyper-parameters that control the data augmentation functions is computationally expensive. Given the drawbacks of consistency learning methods, we explore pseudo-label methods in this paper, but we introduce a mechanism to address the confirmation bias problem.

2.4. Pre-training methods in medical image analysis

Pre-training is an important step whenever the annotated training set is too small to provide a robust model training (Clancy et al., 2020). The most successful pre-training methods are based on ImageNet pre-training (Bar et al., 2015; Carneiro et al., 2017), self-supervised pre-training (Vu et al., 2021), or proxy-task pre-training (Clancy et al., 2020).

ImageNet pre-training (Russakovsky et al., 2015) is widely used in the medical image analysis (Bar et al., 2015; Carneiro et al., 2017), where it can enable faster convergence (Raghu et al., 2019) or compensate for small training sets (Carneiro et al., 2017). However, ImageNet pre-training can be problematic given the fundamental differences in image characteristics between natural images and medical images. **Self-supervised pre-training** (Vu et al., 2021) has shown strong results, but designing an arbitrary self-supervised task that is helpful for the target task (i.e., lesion detection) is not trivial, and self-supervised pre-training tends to be a complex process that can take a significant amount of training time. The use of **proxy-task pre-training** (Clancy et al., 2020) is the method that usually shows the best performance, as long as the proxy task is relevant to the target task. We follow the proxy-task pre-training given its superior performance.

3. Proposed method

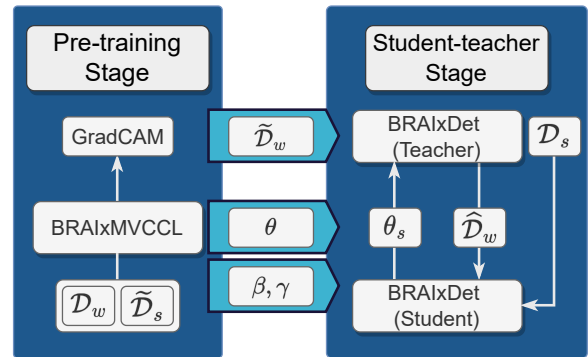


Fig. 2. Overview of the proposed multi-stage training that comprises the pre-training on a weakly-supervised classification task, and a semi-supervised student-teacher learning to detect malignant lesions with incomplete annotations. During pre-training, we train the classifier BRAIxMVCCL using a weakly-labelled version of \mathcal{D}_s , called $\hat{\mathcal{D}}_s$, and \mathcal{D}_w . After pre-training, we transfer two types of information to the next training stage: 1) the set $\hat{\mathcal{D}}_w$ that contains the detected lesions using the GradCAM maps from the classifier applied to the samples in \mathcal{D}_w ; and 2) the BRAIxMVCCL’s parameter θ , and running mean β and standard deviation γ for batch norm layers. The semi-supervised student-teacher learning builds the teacher and student BRAIxDet detectors from BRAIxMVCCL’s parameters, where the student is trained with the fully-supervised \mathcal{D}_s and the pseudo-labelled $\hat{\mathcal{D}}_w$ produced from the teacher’s detections and GradCAM detections in $\hat{\mathcal{D}}_w$, and the teacher is trained with exponential moving average of the student’s parameters.

Problem definition. Our method aims to train an accurate breast lesion detector from a dataset of multi-view (i.e., CC and MLO) mammograms containing incomplete annotations, i.e., a

Table 1. List of Symbols.

Problem Definition	
m	Main view of the system
a	Auxiliary view of the system
\mathcal{D}	Dataset
\mathcal{D}_s	Fully-annotated subset
\mathcal{D}_w	Weakly-annotated subset
\mathcal{Y}	Classification and bounding box labels of the lesions
C	Set of classification labels (with 1 = cancer and 0 = non-cancer)
\mathcal{B}	Domain for the top-left and bottom-right coordinates of the bounding box label
\mathcal{X}	Domain for mammogram images
Pre-training on Multi-view Classification	
$\widetilde{\mathcal{D}}_s$	Weakly-labelled version of \mathcal{D}_s
$\widetilde{\mathcal{D}}_w$	Pseudo-labelled version of \mathcal{D}_w produced by GradCAM
$\widetilde{\mathcal{Y}}$	Classification and bounding box pseudo labels of the lesions produced by MVCCL
θ	MVCCL’s network parameters
γ	Running mean of BatchNorm layers in MVCCL
β	Running variance of BatchNorm layers in MVCCL
\mathbf{u}	Feature map
\mathbf{h}	GradCam heatmap
\mathcal{L}	Set of connected components produced by \mathbf{h}
Student-teacher SSL for Lesion Detection	
$\widetilde{\mathcal{D}}_w$	Pseudo-labelled version of \mathcal{D}_w by teacher network
$\widetilde{\mathcal{Y}}$	Classification and bounding box pseudo labels of the lesions produced by the teacher network
θ_t	Model parameters for teacher network
θ_s	Model parameters for student network
λ	hyper-parameter of weakly-supervised loss
α	Smoothing factor of EMA

dataset composed of a fully-annotated subset \mathcal{D}_s and a weakly-annotated subset \mathcal{D}_w – please note that all symbols used in this paper are defined in Table 1. The fully-annotated subset is denoted by $\mathcal{D}_s = \{\mathbf{x}_i^m, \mathbf{x}_i^a, \mathcal{Y}_i^m\}_{i=1}^{|\mathcal{D}_s|}$, where $\mathbf{x} \in \mathcal{X} \subset \mathbb{R}^{H \times W}$ represents a mammogram of height H and width W , \mathbf{x}_i^m represents the main view, \mathbf{x}_i^a is the auxiliary view (with $m, a \in \{CC, MLO\}$ and $m \neq a$), $\mathcal{Y}_i^m = \{\mathbf{c}_{i,j}^m, \mathbf{b}_{i,j}^m\}_{j=1}^{|\mathcal{Y}_i^m|}$ denotes the classification and localisation of the $|\mathcal{Y}_i^m|$ image lesions, with $\mathbf{c}_{i,j}^m \in C = \{0, 1\}$ denoting the j^{th} lesion label (with 1 = cancer and 0 = non-cancer) and $\mathbf{b}_{i,j}^m \in \mathcal{B} \in \mathbb{R}^4$ representing the top-left and bottom-right coordinates of the bounding box of the j^{th} lesion on \mathbf{x}_i^m . The weakly-annotated subset is defined as $\mathcal{D}_w = \{\mathbf{x}_i^m, \mathbf{x}_i^a, \mathbf{c}_i^m\}_{i=1}^{|\mathcal{D}_w|}$, with $\mathbf{c}_i^m \in C = \{0, 1\}$. The testing set is similarly defined as the fully-annotated subset since we aim to assess the lesion detection performance.

System overview. To effectively utilise the training samples in \mathcal{D}_s and \mathcal{D}_w , we propose a 2-stage learning process, with a weakly-supervised pre-training using all samples from \mathcal{D}_w and $\widetilde{\mathcal{D}}_s =$

$\{(\mathbf{x}_i^m, \mathbf{x}_i^a, \mathbf{c}_i^m) | (\mathbf{x}_i^m, \mathbf{x}_i^a, \mathcal{Y}_i^m) \in \mathcal{D}_s, \text{ and } \mathbf{c}_i^m = \max_{j \in \{1, \dots, |\mathcal{Y}_i^m|\}} (\mathbf{c}_{i,j}^m)\}$, followed by semi-supervised student-teacher learning using \mathcal{D}_s and pseudo-labelled $\widetilde{\mathcal{D}}_w$, as shown in Figure 2. In the **pre-training stage** described in Section 3.1, we train the multi-view mammogram classifier BRAIxMVCCL (Chen et al., 2022) to learn an effective feature extractor and a reasonably accurate GradCAM detector (Selvaraju et al., 2017) to support the next stage of semi-supervised learning. After pre-training, we replace the classification layer of BRAIxMVCCL with a detection head, forming the BRAIxDet model based on the Faster R-CNN backbone (Ren et al., 2015), and we also duplicate BRAIxDet into the student and teacher models. In our **student-teacher semi-supervised learning (SSL)** stage explained in Section 3.2, we train the student and teacher models, where the teacher uses its detector and the GradCAM detections in $\widetilde{\mathcal{D}}_w$ to generate localisation pseudo-labels, denoted by $\widetilde{\mathcal{Y}}_i^m$, for the lesions in the samples $(\mathbf{x}_i^m, \mathbf{x}_i^a, \mathbf{c}_i^m) \in \mathcal{D}_w$, forming the new pseudo-labelled dataset $\widetilde{\mathcal{D}}_w$ to train the student, and the student updates the teacher’s model parameters based on the exponential moving average (EMA) (Laine and Aila, 2016; Tarvainen and Valpola, 2017) of its model parameters. Additionally, the student is also trained to detect lesions using the fully-annotated samples from \mathcal{D}_s .

During **inference**, the final lesion detection results are represented by the bounding box predictions from the **teacher** BRAIxDet model.

3.1. Pre-training on multi-view mammogram classification

We pre-train our previously proposed BRAIxMVCCL model (Chen et al., 2022) on the classification task before transforming it into a Faster R-CNN detector (Ren et al., 2015) to be trained to localise cancerous lesions. The multi-view backbone classifier BRAIxMVCCL (Chen et al., 2022), parameterised by $\theta \in \Theta$ and partially illustrated in Figure 3, is defined by $\hat{\mathbf{c}} = f_\theta(\mathbf{x}^m, \mathbf{x}^a)$, which returns a classification $\hat{\mathbf{c}} \in [0, 1]$ (1 = cancer and 0 = non-cancer) given the main and auxiliary views $\mathbf{x}^m, \mathbf{x}^a$. This model is trained with $\widetilde{\mathcal{D}}_s$ and \mathcal{D}_w defined above to minimise classification mistakes and maximise the consistency between the global image features produced from each view, as follows:

$$\theta^* = \arg \min_{\theta \in \Theta} \sum_{(\mathbf{x}_i^m, \mathbf{x}_i^a, \mathbf{c}_i^m) \in \mathcal{D}_w \cup \widetilde{\mathcal{D}}_s} \ell_{bce}(f_\theta(\mathbf{x}_i^m, \mathbf{x}_i^a), \mathbf{c}_i^m) + \ell_{sim}(f_\theta^g(\mathbf{x}_i^m), f_\theta^g(\mathbf{x}_i^a)), \quad (1)$$

where $\ell_{bce}(\cdot)$ denotes the binary cross-entropy (BCE) loss, and $\ell_{sim}(\cdot)$ denotes the consistency loss between the global features produced by $f_\theta^g(\cdot)$, which is part of the model $f_\theta(\cdot)$.

A particularly important structure from the BRAIxMVCCL classifier, which will be useful for the detector BRAIxDet, is the local co-occurrence module (LCM) that explores the cross-view feature relationships at local regions for the main view image \mathbf{x}^m . The LCM is denoted by $\tilde{\mathbf{u}}^m = \mathbf{u}^m \oplus f_\theta^l(\mathbf{u}^m, \mathbf{u}^a)$, where $\tilde{\mathbf{u}}^m \in \mathbb{R}^{\hat{H} \times \hat{W} \times D'}$ (with $\hat{H} < H$ and $\hat{W} < W$), \oplus denotes the concatenation operator, and $f_\theta^l(\cdot)$ is part of $f_\theta(\cdot)$. The features used

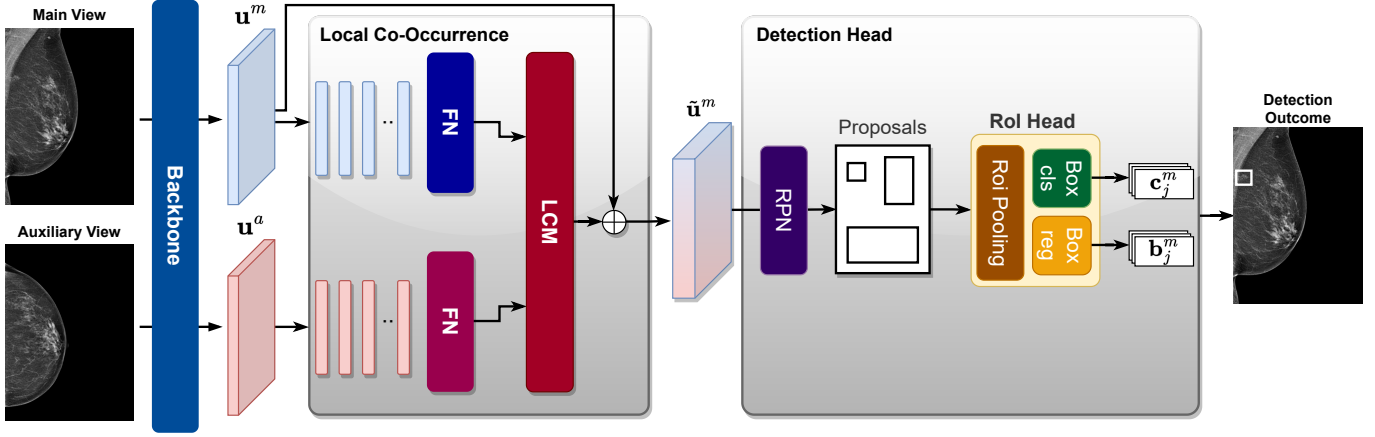


Fig. 3. BRAIDet takes two mammographic views (main and auxiliary) and uses a backbone model to extract the main and auxiliary features u^m and u^a , where the main components are: 1) the local co-occurrence module (LCM) that models the local semantic relationships between the two views to output the cross-view feature \tilde{u}^m ; and 2) the detection module that outputs the classifications $\{c_j^m\}_{j=1}^{|\mathcal{Y}^m|}$ and lesion bounding box predictions $\{b_j^m\}_{j=1}^{|\mathcal{Y}^m|}$. FN stands for fully-connected layers, \oplus indicates the concatenation operator, and RPN is the region proposal network.

Algorithm 1 Produce GradCAM pseudo-labelled dataset $\tilde{\mathcal{D}}_w$

- 1: **require:** Weakly-supervised dataset \mathcal{D}_w , BRAIXMVCCCL model $f_\theta(\cdot)$, and threshold τ
- 2: $\tilde{\mathcal{D}}_w = \emptyset$ ▷ Initialise pseudo-labelled $\tilde{\mathcal{D}}_w$
- 3: **for** $(\mathbf{x}_i^m, \mathbf{x}_i^a, \mathbf{c}_i) \in \mathcal{D}_w$, where $\mathbf{c}_i = 1$ **do**
- 4: $\hat{\mathbf{c}}_i = f_\theta(\mathbf{x}_i^m, \mathbf{x}_i^a)$
- 5: $\mathbf{h}_i = \text{GradCAM}(f_\theta(\mathbf{x}_i^m, \mathbf{x}_i^a), \mathbf{c}_i)$ ▷ Heatmap prediction
- 6: $\hat{\mathbf{h}}_i = \mathbb{I}(\mathbf{h}_i > \tau) \odot \mathbf{h}_i$ ▷ Binarise heatmap
- 7: $\mathcal{L}_i = \text{CCA}(\hat{\mathbf{h}}_i)$ ▷ Connected component analysis
- 8: **for** $\mathbf{l}_j \in \mathcal{L}_i$ **do** ▷ Remove small and large components
- 9: **if** $\text{area}(\mathbf{l}_j) < 32 \times 32$ **then** $\mathcal{L}_i \leftarrow \mathcal{L}_i \setminus \mathbf{l}_j$
- 10: **if** $\text{area}(\mathbf{l}_j) > 1024 \times 1024$ **then** $\mathcal{L}_i \leftarrow \mathcal{L}_i \setminus \mathbf{l}_j$
- 11: $\tilde{\mathcal{Y}}_i^m = \emptyset$ ▷ GradCAM detections
- 12: **for** $\mathbf{l}_j \in \mathcal{L}_i$ **do**
- 13: $\mathbf{b}_j = \text{BBox}(\mathbf{l}_j)$ ▷ Get bounding box from \mathbf{l}_j
- 14: $\tilde{\mathcal{Y}}_i^m \leftarrow \tilde{\mathcal{Y}}_i^m \cup (\hat{\mathbf{c}}_i, \mathbf{b}_j)$ ▷ Add bounding box to $\tilde{\mathcal{Y}}_i^m$
- 15: $\tilde{\mathcal{D}}_w \leftarrow \tilde{\mathcal{D}}_w \cup (\mathbf{x}_i^m, \mathbf{x}_i^a, \tilde{\mathcal{Y}}_i^m)$
- 16: **return** $\tilde{\mathcal{D}}_w$

by LCM are extracted from $\mathbf{u}^m = f_\theta^b(\mathbf{x}^m)$ and $\mathbf{u}^a = f_\theta^b(\mathbf{x}^a)$, where $f_\theta^b(\cdot)$ is also part of $f_\theta(\cdot)$ and $\mathbf{u}^m, \mathbf{u}^a \in \mathcal{U} \subset \mathbb{R}^{\hat{H} \times \hat{W} \times D}$ (with $D > D'$).

The student-teacher SSL stage will require the detection of pseudo labels for the weakly supervised dataset \mathcal{D}_w . To avoid the confirmation bias described in Section 2.3, we combine the teacher’s detection results, explained below in Section 3.2, with the GradCAM (Selvaraju et al., 2017) detections for the cancer cases produced by the BRAIXMVCCCL classifier. Algorithm 1 displays the pseudo-code to generate GradCAM pseudo labels, where $\text{GradCAM}(f_\theta(\mathbf{x}_i^m, \mathbf{x}_i^a), \mathbf{c}_i)$ returns the GradCAM heatmap $\mathbf{h}_i \in [0, 1]^{H \times W}$ for class \mathbf{c}_i on image \mathbf{x}_i^m , $\mathbb{I}(\mathbf{h}_i > \tau)$ produces a binary map with the heatmap pixels larger than τ being set to 1 or 0 otherwise, \odot denotes the element-wise multiplication operator, $\text{CCA}(\mathbf{h}_i)$ produces the set of connected components $\mathcal{L}_i = \{\mathbf{l}_j\}_{j=1}^{|\mathcal{L}_i|}$ from the binarised heatmap $\hat{\mathbf{h}}_i$ (with $\mathbf{l}_j \in \{0, 1\}^{H \times W}$),

$\text{area}(\mathbf{l}_j)$ returns the area (i.e., number of pixels $\omega \in \Omega$ where $\mathbf{l}_j(\omega) = 1$, where Ω is the image lattice) of the connected component \mathbf{l}_j , and $\text{BBox}(\mathbf{l}_j)$ returns the 4 coordinates of the bounding box \mathbf{b}_j from the (left, right, top, bottom) bounds of connected component \mathbf{l}_j . This prediction process produces a set of bounding boxes paired with the confidence score $\hat{\mathbf{c}}_i$ from classifier BRAIXMVCCCL (Chen et al., 2022), forming $\tilde{\mathcal{Y}}_i^m = \{(\hat{\mathbf{c}}_i, \mathbf{b}_j)\}_{j=1}^{|\mathcal{Y}_i^m|}$ for each training sample.

3.2. Student-teacher SSL for lesion detection

After pre-training, we modify the structure of the trained BRAIXMVCCCL model (Chen et al., 2022) $f_\theta(\mathbf{x}_i^m, \mathbf{x}_i^a)$ by pruning the global consistency module (GCM) denoted by $f_\theta^g(\cdot)$, the classification layers, and the part of the local co-occurrence module (LCM) that produces spatial attention for the auxiliary image since these layers do not provide useful information for lesion localisation in the main image. This pruning process is followed by the addition of the detection head (Ren et al., 2015), consisting of the region proposal network (RPN) and region of interest (RoI-head) head, which forms the detector $\tilde{\mathcal{Y}}_i^m = f_\theta^d(\mathbf{x}_i^m, \mathbf{x}_i^a)$, where $\tilde{\mathcal{Y}}_i^m = \{(\hat{\mathbf{c}}_{i,j}^m, \hat{\mathbf{b}}_{i,j}^m)\}_{j=1}^{|\hat{\mathcal{Y}}_i^m|}$, with $\hat{\mathbf{c}}_{i,j}^m \in [0, 1]$ and $\hat{\mathbf{b}}_{i,j}^m \in \mathcal{B} \subset \mathbb{R}^4$. Then, we duplicate this model into a teacher $f_\theta^d(\mathbf{x}_i^m, \mathbf{x}_i^a)$ and a student $f_\theta^d(\mathbf{x}_i^m, \mathbf{x}_i^a)$ that are used in the SSL training (Tarvainen and Valpola, 2017), where we train the student with the fully-labelled \mathcal{D}_s and the pseudo-labelled $\tilde{\mathcal{D}}_w$, while the teacher network is trained with the exponential moving average (EMA) of the student’s parameters (Tarvainen and Valpola, 2017). Figure 3 shows the BRAIDet structure, and Figure 4 summarises the student-teacher SSL training stage.

For the supervised training of the student, we followed the Faster-RCNN training procedure that consists of four loss functions to train the RPN and RoI-head modules to classify bounding boxes and regress their coordinates (Ren et al., 2015). The

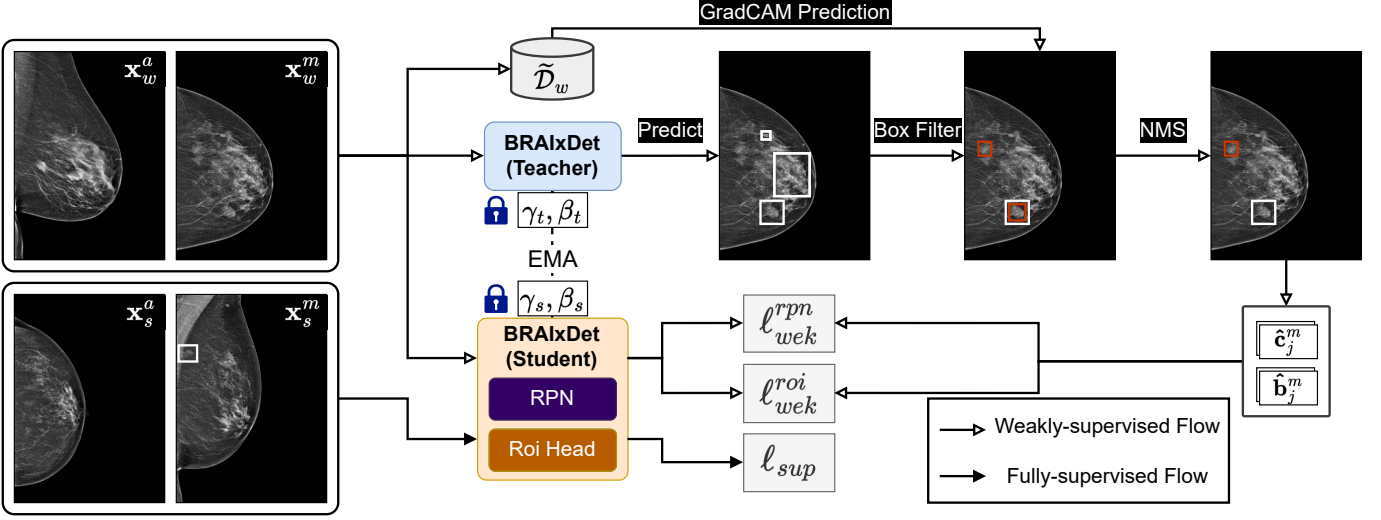


Fig. 4. The student-teacher SSL of our BRAIxDet is optimised in two steps: 1) the student is trained with the fully-annotated \mathcal{D}_s , using loss $\ell_{sup}(\cdot)$ in (2), and with the pseudo-labelled $\hat{\mathcal{D}}_w$ produced by the teacher and GradCAM predictions in $\tilde{\mathcal{D}}_w$ for the weakly supervised dataset \mathcal{D}_w ; and 2) the teacher network is updated based on the EMA of the student’s network parameters. We introduce the following two steps to improve the quality of the pseudo labels produced by the teacher: a) a box filtering process that selects the teacher’s most confident prediction; b) a non-maximum suppression (NMS) operation that rejects duplicated boxes by comparing the overlap and objectiveness score between the most confident of the teacher’s predictions and the GradCAM predictions. The running mean γ and standard deviation β for both the batch normalisation of the teacher and student models are fixed during the entire process.

Algorithm 2 Non-maximum Suppression (NMS)

- 1: **require:** $\mathcal{B} = \{b_1, \dots, b_n\}$, $\mathcal{S} = \{s_1, \dots, s_n\}$, τ_{nms}
 \mathcal{B} is a set of predicted bounding boxes.
 \mathcal{S} contains corresponding detection scores.
 τ_{nms} : represent the IoU threshold.
- 2: $\hat{\mathcal{Y}} \leftarrow \emptyset$
- 3: **while** $\mathcal{B} \neq \emptyset$ **do**
- 4: $i_{max} \leftarrow \arg \max_{i \in \{1, \dots, |\mathcal{S}|\}} s_i \in \mathcal{S}$
- 5: $\hat{\mathcal{Y}} \leftarrow \hat{\mathcal{Y}} \cup (b_{i_{max}}, s_{i_{max}})$
- 6: $\mathcal{B} \leftarrow \mathcal{B} - b_{i_{max}}$
- 7: $\mathcal{S} \leftarrow \mathcal{S} - s_{i_{max}}$
- 8: **for** $i \in \{1, \dots, |\mathcal{B}|\}$ **do**
- 9: **if** $IoU(b_{i_{max}}, b_i) \geq \tau_{nms}$ **then**
- 10: $\mathcal{B} \leftarrow \mathcal{B} - b_i$
- 11: $\mathcal{S} \leftarrow \mathcal{S} - s_i$
- 12: **return** $\hat{\mathcal{Y}}$

objective function is defined as

$$\begin{aligned} \ell_{sup}(\mathcal{D}_s, \theta_s) = & \sum_{(\mathbf{x}_i^m, \mathbf{x}_i^a, \mathcal{Y}_i^m) \in \mathcal{D}_s} \left(\ell_{cls}^{rpn}(f_{\theta_s}^d(\mathbf{x}_i^m, \mathbf{x}_i^a), \mathcal{Y}_i^m) + \ell_{reg}^{rpn}(f_{\theta_s}^d(\mathbf{x}_i^m, \mathbf{x}_i^a), \mathcal{Y}_i^m) \right) + \\ & \sum_{(\mathbf{x}_i^m, \mathbf{x}_i^a, \mathcal{Y}_i^m) \in \mathcal{D}_s} \left(\ell_{cls}^{roi}(f_{\theta_s}^d(\mathbf{x}_i^m, \mathbf{x}_i^a), \mathcal{Y}_i^m) + \ell_{reg}^{roi}(f_{\theta_s}^d(\mathbf{x}_i^m, \mathbf{x}_i^a), \mathcal{Y}_i^m) \right), \end{aligned} \quad (2)$$

where $\ell_{cls}^{rpn}(\cdot)$, $\ell_{reg}^{rpn}(\cdot)$ denote the RPN classification and regression losses with respect to the anchors, and $\ell_{cls}^{roi}(\cdot)$, $\ell_{reg}^{roi}(\cdot)$ represent the ROI-head classification and regression losses with respect to the region proposal features (Ren et al., 2015).

These pseudo-labels to train the student are provided by

the teacher, which form the pseudo-labelled dataset $\hat{\mathcal{D}}_w = \{(\mathbf{x}_i^m, \mathbf{x}_i^a, \hat{\mathcal{Y}}_i^m) | (\mathbf{x}_i^m, \mathbf{x}_i^a, \mathcal{C}_i^m) \in \mathcal{D}_w, \text{ and } \hat{\mathcal{Y}}_i^m = f_{\theta_t}^d(\mathbf{x}_i^m, \mathbf{x}_i^a)\}$. However, at the beginning of the training (first two training epochs), the pseudo-labels in $\hat{\mathcal{D}}_w$ are unreliable, which can cause the confirmation bias issue mentioned in Section 2.3, so we also use the GradCAM predictions in $\tilde{\mathcal{D}}_w$ from Algorithm 1. More specifically, starting from $(\mathbf{x}_i^m, \mathbf{x}_i^a, \mathcal{Y}_i^m) \in \tilde{\mathcal{D}}_w$, we first select the most confident prediction from $(\hat{\mathbf{c}}_{i,j}^m, \hat{\mathbf{b}}_{i,j}^m) \in \mathcal{Y}_i^m$, with $j^* = \arg \max_{j \in \{1, \dots, |\mathcal{Y}_i^m|\}} \hat{\mathbf{c}}_{i,j}^m$, and add it to the set of GradCAM detections in $\hat{\mathcal{Y}}_i^m$. Then, for each training sample $(\mathbf{x}_i^m, \mathbf{x}_i^a, \mathcal{Y}_i^m) \in \tilde{\mathcal{D}}_w$ we run non-max suppression (NMS, as shown in Algorithm 2) on the teacher and GradCAM detections to form $\hat{\mathcal{Y}}_i^m \leftarrow NMS(\mathcal{Y}_i^m \cup (\hat{\mathbf{c}}_{i,j^*}^m, \hat{\mathbf{b}}_{i,j^*}^m))$. After these initial training stages, the pseudo-label is solely based on the teacher’s prediction from $\hat{\mathcal{D}}_w$. The objective function to train the student using $\hat{\mathcal{D}}_w$ is defined as

$$\begin{aligned} \ell_{wek}(\hat{\mathcal{D}}_w, \theta_s) = & \sum_{(\mathbf{x}_i^m, \mathbf{x}_i^a, \mathcal{Y}_i^m) \in \hat{\mathcal{D}}_w} \left(\ell_{cls}^{rpn}(f_{\theta_s}^d(\mathbf{x}_i^m, \mathbf{x}_i^a), \mathcal{Y}_i^m) + \ell_{reg}^{rpn}(f_{\theta_s}^d(\mathbf{x}_i^m, \mathbf{x}_i^a), \mathcal{Y}_i^m) \right) + \\ & \sum_{(\mathbf{x}_i^m, \mathbf{x}_i^a, \mathcal{Y}_i^m) \in \hat{\mathcal{D}}_w} \left(\ell_{cls}^{roi}(f_{\theta_s}^d(\mathbf{x}_i^m, \mathbf{x}_i^a), \mathcal{Y}_i^m) + \ell_{reg}^{roi}(f_{\theta_s}^d(\mathbf{x}_i^m, \mathbf{x}_i^a), \mathcal{Y}_i^m) \right), \end{aligned} \quad (3)$$

where the losses used here are the same as the ones in (2).

The overall loss function to train the student is

$$\ell_{stu}(\mathcal{D}_s, \hat{\mathcal{D}}_w, \theta_s) = \ell_{sup}(\mathcal{D}_s, \theta_s) + \lambda \ell_{wek}(\hat{\mathcal{D}}_w, \theta_s), \quad (4)$$

where λ is the hyper-parameter that controls the contribution of the weakly-supervised loss. The teacher’s model parameters

are updated with EMA (Tarvainen and Valpola, 2017):

$$\theta'_t = \alpha\theta_t + (1 - \alpha)\theta_s, \quad (5)$$

where $\alpha \in (0, 1)$ is a hyper-parameter that represents the smoothing factor, where a high value of α provides a slow updating process.

3.3. Batch Normalisation for EMA

In the original mean-teacher training (Tarvainen and Valpola, 2017), both student and teacher use the standard batch normalization (BN). For the student network, the model parameter θ_s is aligned with the BN parameters γ and standard deviation β since these parameters are optimized based on the batch-wise statistics. However, this relationship does not hold for the teacher’s network since the teacher’s model parameter θ_t is updated by EMA, but the BN statistics are not updated. Cai et al. (2021) claimed that this issue can be solved by applying EMA on BN statistics to avoid the misalignment in the teacher’s parameter space. We propose a simpler approach to address this issue, which is to simply freeze the BN layers for both student and teacher models since the BN statistics is already well estimated from the entire dataset $\tilde{\mathcal{D}}_s \cup \mathcal{D}_w$ during pre-training. We show in the experiments that our proposal above addresses well the mismatch between the student’s and the teacher’s parameters and the dependency on the student’s training samples, providing better detection generalisation than presented by Cai et al. (2021).

4. Experiments

In this section, we first introduce the two datasets used in the experiments, and then we explain the experimental setting containing variable proportions of fully and weakly annotated samples in the training set. Next, we discuss the implementation details of our method and competing approaches. We conclude the section with a visualization of the detection results and ablation studies.

4.1. Datasets

We validate our proposed BRAIxDet method on two datasets that contain incomplete malignant breast lesion annotations, namely: our own Annotated Digital Mammograms and Associated Non-Image data (ADMANI), and the public Curated Breast Imaging Subset of the Digital Database for Screening Mammography (CBIS-DDSM) (Lee et al., 2017).

The **ADMANI Dataset** was collected from several breast screening clinics from the State of Victoria in Australia, between 2013 and 2019, and contains pre-defined training and testing sets. Each exam on ADMANI has two mammographic views (CC and MLO) per breast produced by one of the following manufactures: SiemensTM, HologicTM, Fujifilm CorporationTM, PhilipsTM Digital Mammography Sweden AB, Konica MinoltaTM, GETM Medical Systems, Philips Medical SystemsTM, and AgfaTM. The training set contains 771,542 exams with 15,994 cancer cases (containing malignant findings) and 3,070,174 non-cancer cases (with 44,040 benign cases and

3,026,134 cases with no findings). This training set is split 90/10 for training/validation in a patient-wise manner. The training set has 7,532 weakly annotated cancer cases and 6,892 fully annotated cancer cases, while the validation set has 759 fully annotated cancer cases and no weakly annotated cases since they are not useful for model selection. The testing set contains 83,990 exams with 1,262 cancer cases (containing malignant findings) and 334,698 non-cancer cases (with 3,880 benign cases and 330,818 no findings). Given that we are testing lesion detection, we remove all non-cancer cases, and all weakly annotated cancer cases, leaving us with 900 fully annotated cancer cases.

The **publicly available CBIS-DDSM dataset** (Lee et al., 2017) contains images from 1,566 participants, where 1,457 cases have malignant findings (with 1,696 mass cases and 1,872 calcification cases). The dataset has a pre-defined training and testing split, with 2,864 images (with 1,181 malignant cases and 1,683 benign cases) and 704 (with 276 malignant cases and 428 benign cases) images respectively. Each exam on CBIS-DDSM also has two mammographic views (CC and MLO) per breast.

4.2. Experimental settings

To systematically test the robustness of our method to different rates of incomplete malignant breast lesion annotations, we propose an experimental setting that contains different proportions of fully- and weakly-annotated samples. In the **partially labelled protocol**, we follow typical semi-supervised settings (Sohn et al., 2020; Liu et al., 2021; Xu et al., 2021; Liu et al., 2022), where we sub-sample the fully-annotated subset using the ratio $1/n$, where the remaining $1 - 1/n$ of the subset becomes weakly-annotated. More specifically, on ADMANI, we split the fully-annotated subset with the ratios $3/4$, $1/2$, $1/4$, $1/8$, $1/16$. We adopt the same experimental setting for CBIS-DDSM (Lee et al., 2017). In the **fully labelled protocol**, we use all ADMANI training samples that have the lesion localisation annotation as the fully-annotated subset and all remaining weakly-labelled samples as the weakly-annotated subset. Unlike the synthetic partially labelled protocol setting, the fully labelled protocol setup is a real-world challenge since it uses all data available from ADMANI, allowing methods to leverage all the available samples to improve detector performance on a large-scale mammogram dataset.

All methods are assessed using the standard **mean average precision (mAP)** and **free-response receiver operating characteristic (FROC)**. The mAP measures the average precision of true positive (TP) detections of malignant lesions, where a TP detection is defined as producing at least a 0.2 intersection over union (IoU) with respect to the bounding box annotation (Liu et al., 2020b; Yang et al., 2020, 2021). We follow previous works (Dhungel et al., 2017; Agarwal et al., 2020; Liu et al., 2019, 2020b; Yang et al., 2021) when selecting a threshold of 0.2 for testing, due to the following reasons: 1) large overlaps between annotations and detections that do not happen as often as in natural images since mammograms represent a compressed and thin 3D space compared to natural images (Ribli et al., 2018), resulting in lesions that occupy a rather small region of the image; and 2) inconsistent annotation quality where ground-truth labels can be much larger/smaller than

Table 2. mAP and Recall @ 0.5 results on the testing images of ADMANI (Frazer et al., 2022) using the partially labelled protocol based on splitting the fully annotated subset with the ratios 1/16, 1/8, 1/4, 1/2, and 3/4 (we show the number of fully annotated images inside the brackets). We highlight the best result in each column. The last row shows the p -values from the one-tailed t-test to compare our BRAIxDet against the second best method (Soft Teacher (Xu et al., 2021)).

Method	mAP					Recall @ 0.5				
	1/16 (430)	1/8 (861)	1/4 (1723)	1/2 (3446)	3/4 (5169)	1/16 (430)	1/8 (861)	1/4 (1723)	1/2 (3446)	3/4 (5169)
Faster RCNN (Ren et al., 2015)	61.88 ± 0.64	70.63 ± 0.71	75.49 ± 0.74	80.87 ± 0.81	82.01 ± 0.67	62.33 ± 0.80	72.15 ± 0.52	76.77 ± 0.58	81.41 ± 0.76	82.27 ± 0.78
CVR-RCNN (Ma et al., 2021)	62.99 ± 0.83	71.13 ± 0.80	76.32 ± 0.69	81.94 ± 0.86	83.09 ± 0.93	63.29 ± 0.67	73.17 ± 0.66	77.48 ± 0.57	82.55 ± 0.64	83.25 ± 0.70
MommiNet-V2 (Yang et al., 2021)	63.64 ± 0.75	72.51 ± 0.93	77.21 ± 0.76	82.52 ± 0.79	84.07 ± 0.81	63.72 ± 0.93	74.25 ± 0.59	78.05 ± 0.89	83.48 ± 0.75	83.85 ± 0.67
STAC (Sohn et al., 2020)	73.89 ± 0.80	79.18 ± 0.95	81.98 ± 0.89	84.32 ± 0.71	85.21 ± 0.76	74.70 ± 0.81	82.66 ± 0.77	87.13 ± 0.64	88.16 ± 0.52	89.42 ± 0.58
MT (Tarvainen and Valpola, 2017)	78.21 ± 0.81	78.96 ± 0.99	85.78 ± 0.82	86.52 ± 0.75	87.82 ± 0.69	81.66 ± 0.92	85.50 ± 0.60	90.67 ± 0.76	90.30 ± 0.62	91.12 ± 0.68
Unbiased Teacher (Liu et al., 2021)	63.57 ± 0.67	75.87 ± 0.72	81.04 ± 0.61	82.17 ± 0.83	83.82 ± 0.68	64.31 ± 0.71	79.41 ± 0.59	84.38 ± 0.61	85.05 ± 0.74	86.23 ± 0.72
Soft Teacher (Xu et al., 2021)	81.84 ± 0.91	83.46 ± 0.83	85.96 ± 0.75	86.75 ± 0.89	87.74 ± 0.64	85.92 ± 0.59	89.38 ± 0.67	89.98 ± 0.61	90.69 ± 0.79	91.77 ± 0.59
BRAIxDet	88.34 ± 0.61	89.10 ± 0.62	90.57 ± 0.79	91.84 ± 0.75	92.33 ± 0.62	91.21 ± 0.46	92.73 ± 0.74	93.58 ± 0.56	94.08 ± 0.66	94.88 ± 0.57
BRAIxDet (p-value)	< 1e-14	< 1e-14	< 1e-14	< 1e-14	< 1e-14	< 1e-14	< 1e-14	< 1e-14	< 1e-14	< 1e-14

Table 3. mAP and Recall @ 0.5 results on the testing images of ADMANI (Frazer et al., 2022) using the fully labelled protocol based on all fully annotated data and extra weakly-labelled data (we show the number of extra weakly labelled images inside the brackets). We highlight the best result in each column.

Method	100%+Extra (6298)	
	mAP	Recall @ 0.5
Faster RCNN (Ren et al., 2015)	84.52 ± 0.65	85.09 ± 0.69
CVR-RCNN (Ma et al., 2021)	85.52 ± 0.60	86.03 ± 0.84
MommiNet-V2 (Yang et al., 2021)	85.91 ± 0.89	86.87 ± 0.95
STAC (Sohn et al., 2020)	88.82 ± 0.78	92.49 ± 0.58
MT (Tarvainen and Valpola, 2017)	89.11 ± 1.01	92.22 ± 0.62
Unbiased Teacher (Liu et al., 2021)	87.17 ± 0.61	92.48 ± 0.95
Soft Teacher (Xu et al., 2021)	90.29 ± 0.88	92.71 ± 0.91
BRAIxDet	92.78 ± 0.78	95.18 ± 0.68

its actual size, which may cause inaccurate evaluation. On the other hand, FROC measures the recall at different false positive detections per image (FPPI). In this paper, we measure the recall at 0.5 FPPI (Recall @ 0.5), which means the recall at which the detector produces one false positive every two images. Such Recall@0.5 is a common measure to assess lesion detection from mammograms (Ma et al., 2021; Yang et al., 2020, 2021).

4.3. Implementation details

We **pre-process each image** to remove text annotations and background noise outside the breast region, then we crop the area outside the breast region and pad the pre-processed images, such that their H/W has the ratio 1536/768 pixels. During data loading, we resize the input images to 1536 x 768 pixels and flip the images, so that the nipple is located on the right-hand side of the image. For the **pre-training**, we implement the classifier BRAIxMVCCCL (Chen et al., 2022) with the EfficientNet-b0 (Tan and Le, 2019) backbone, initialized with ImageNet-trained (Russakovsky et al., 2015) weights. Our pre-training relies on the Adam optimiser (Kingma and Ba, 2014) using a learning rate of 0.0001, weight decay of 10^{-6} , batch size of 8 images and 20 epochs. The **semi-supervised student-teacher learning** first updates the classi-

fier BRAIxMVCCCL (Chen et al., 2022) into the proposed detector BRAIxDet using the Faster R-CNN (Ren et al., 2015) backbone. We set the binarising threshold τ in Algorithm 1 to 0.5. We follow the default Faster R-CNN hyper-parameter setting from the Torchvision Library (Paszke et al., 2019), except for the NMS threshold that was reduced to 0.2 and for the TP IoU detection for `Roi_head` which was set to 0.2. The optimization of BRAIxDet also relies on Adam optimiser (Kingma and Ba, 2014) using a learning rate of 0.00005, weight decay of 10^{-5} , batch size of 4 images and 20 epochs. Similarly to previous papers (Tarvainen and Valpola, 2017; Liu et al., 2021), we set λ , in the overall student loss of (4), to 0.25, and α in the EMA to update the teacher’s parameter in (5) to 0.999. For the pre-training and student-teacher learning stages, we use ReduceLROnPlateau to dynamically control the learning rate reduction based on the BCE loss during model validation, where the reduction factor is set to 0.1.

We compare our method to the following state-of-the-art (SOTA) approaches: Faster RCNN (Ren et al., 2015)¹, STAC (Sohn et al., 2020)², MT (Tarvainen and Valpola, 2017)³, Unbiased Teacher (Liu et al., 2021)⁴, and Soft Teacher (Xu et al., 2021)⁵. All these competing methods’ results are produced by running the code available from their official GitHub repository. We additionally evaluate two malignant breast lesion detection methods: CVR-RCNN (Ma et al., 2021) and MommiNet-V2 (Yang et al., 2021) based on the Relation-Network (Hu et al., 2018)⁶. Please note that we did not implement *nipple detector* and *image reg* modules in MommiNet-V2 (Yang et al., 2021) due to a lack of details in their papers for reproduction.

We ran each experiment three times and formatted results in mean ± standard deviation. These methods are implemented using Faster RCNN with EfficientNet-b0 (Tan and Le, 2019) backbone, pre-trained on the ADMANI dataset using the fully- and weakly-annotated training subsets, following the

¹<https://github.com/pytorch/vision>

²https://github.com/google-research/ssl_detection

³<https://github.com/CuriousAI/mean-teacher>

⁴<https://github.com/facebookresearch/unbiased-teacher>.

⁵<https://github.com/microsoft/SoftTeacher>

⁶https://github.com/heefe92/Relation_Networks-pytorch

Table 4. mAP and Recall @ 0.5 results on the testing images of CBIS-DDSM (Smith, 2017) using the partially labelled protocol based on splitting the fully annotated subset with the ratios 1/16, 1/8, 1/4, 1/2, 3/4 (we show the number of fully annotated images inside the brackets). We highlight the best result in each column. The last row shows the p -values from the one-tailed t-test to compare our BRAIDet against the second best method (Soft Teacher (Xu et al., 2021)).

Method	mAP					Recall @ 0.5				
	1/16 (65)	1/8 (130)	1/4 (260)	1/2 (520)	3/4 (780)	1/16 (65)	1/8 (130)	1/4 (260)	1/2 (520)	3/4 (780)
Faster RCNN (Ren et al., 2015)	24.68 ± 0.52	42.35 ± 0.75	49.55 ± 0.47	54.33 ± 0.72	56.01 ± 0.65	36.78 ± 0.57	54.35 ± 0.66	61.55 ± 0.59	66.64 ± 0.61	70.89 ± 0.74
CVR-RCNN (Ma et al., 2021)	25.86 ± 0.63	42.94 ± 0.88	50.05 ± 0.81	55.12 ± 0.63	61.92 ± 0.82	37.12 ± 0.89	55.56 ± 0.36	62.32 ± 0.67	70.39 ± 0.58	72.52 ± 0.67
MommiNet-V2 (Yang et al., 2021)	26.22 ± 0.79	43.75 ± 0.84	50.82 ± 0.56	59.68 ± 0.71	65.88 ± 0.66	37.94 ± 0.76	56.22 ± 0.62	63.32 ± 0.87	72.73 ± 0.78	75.62 ± 0.65
MT (Tarvainen and Valpola, 2017)	23.31 ± 0.51	33.77 ± 0.45	56.61 ± 0.63	64.59 ± 0.78	66.22 ± 0.82	44.02 ± 0.94	45.32 ± 0.81	64.48 ± 0.73	74.05 ± 0.82	75.94 ± 0.69
STAC (Sohn et al., 2020)	29.16 ± 0.62	45.91 ± 0.73	56.78 ± 0.67	65.54 ± 0.65	66.47 ± 0.77	45.05 ± 0.74	61.65 ± 0.92	71.64 ± 0.65	77.58 ± 0.89	78.15 ± 0.82
Unbiased Teacher (Liu et al., 2021)	36.19 ± 0.66	50.38 ± 0.57	58.83 ± 0.81	65.05 ± 0.51	67.52 ± 0.58	53.78 ± 0.58	62.39 ± 0.61	69.18 ± 0.51	76.18 ± 0.62	77.47 ± 0.55
Soft Teacher (Xu et al., 2021)	45.59 ± 0.70	48.96 ± 0.85	62.03 ± 0.91	67.61 ± 0.80	68.12 ± 0.49	57.91 ± 0.73	65.98 ± 0.66	71.27 ± 0.58	79.20 ± 0.71	81.12 ± 0.82
BRAIDet	53.99 ± 0.83	65.29 ± 0.61	69.32 ± 0.78	72.32 ± 0.66	73.38 ± 0.72	65.84 ± 0.91	72.50 ± 0.44	76.45 ± 0.68	81.82 ± 0.79	83.16 ± 0.57
BRAIDet (p-value)	< 1e-14	< 1e-14	< 1e-14	< 1e-14	< 1e-14	< 1e-14	< 1e-14	< 1e-14	0.0005	0.0002

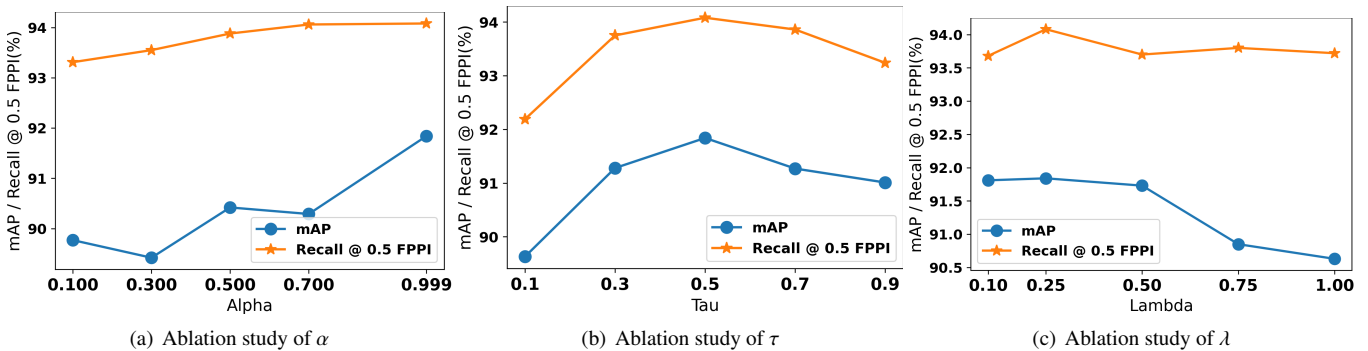


Fig. 5. Ablation study of BRAIDet’s hyper-parameters using mAP and Recall @ 0.5 results on ADMANI dataset (Frazer et al., 2022) under 50% partially labelled protocol. The hyper-parameters include: (a) the smoothing factor α in EMA process; (b) the threshold τ used to binarise the heatmap (Alg. 1); and (c) the weighting factor λ that controls the contribution of the weakly supervised loss.

Table 5. mAP and Recall @ 0.5 results on the testing images of ADMANI (Frazer et al., 2022) and CBIS-DDSM (Smith, 2017) using only the supervised data.

Method	ADMANI		DDSM	
	mAP	Recall @ 0.5	mAP	Recall @ 0.5
Faster RCNN (Ren et al., 2015)	84.52 ± 0.65	85.09 ± 0.69	64.29 ± 0.77	76.86 ± 0.69
CVR-RCNN (Ma et al., 2021)	85.52 ± 0.60	86.03 ± 0.84	69.75 ± 0.78	82.01 ± 0.57
MommiNet-V2 (Yang et al., 2021)	85.91 ± 0.89	86.87 ± 0.95	72.65 ± 0.81	83.40 ± 0.74
BRAIDet	88.68 ± 0.57	91.48 ± 0.74	74.79 ± 0.62	84.88 ± 0.71
BRAIDet (p-value)	0.0009	2e-10	0.0003	0.0186

same setup as our BRAIDet. After pre-training, while Faster RCNN is trained using only the fully-annotated subset, all other methods are trained with both the fully- and weakly-annotated training subsets.

All experiments are implemented with Pytorch (Paszke et al., 2019) and conducted on an NVIDIA A40 GPU (48GB), where training takes about 30 hours on ADMANI and 8 hours on DDSM (Smith, 2017), and testing takes about 0.1s per image. Given that the competing methods use Faster RCNN with the same backbone (EffientNet-b0) as ours and rely on pre-training, their training and testing running times are similar to ours.

4.4. Results

We first present the results produced by our BRAIDet and competing approaches using the partially labelled protocol on

Table 6. Influence of each stage of our method using mAP and Recall @ 0.5 results on ADMANI dataset (Frazer et al., 2022) under fully-labelled protocol. 1st row: Original GradCAM result. 2nd row: Faster RCNN (Ren et al., 2015) with its EfficientNet-b0 backbone pre-trained with fully- and weakly-annotated subsets and trained using only the fully-annotated subset. 3rd row: pre-train the multi-view BRAIMVCCl classifier (Chen et al., 2022), and keep the LCM module for the second training stage that uses the fully-annotated training subset. 4th row: train Faster RCNN with the student-teacher SSL using a backbone without LCM. 5th row: integrate Faster RCNN, LCM and student-teacher SSL. 6th row: BRAIDet results using the BRAIMVCCl’s GradCAM predictions.

Faster RCNN	MV	Studen-teacher	CAM	mAP	Recall @ 0.5
			✓	34.23 ± 0.72	38.18 ± 0.94
✓				84.52 ± 0.65	85.09 ± 0.69
✓	✓			90.05 ± 0.89	93.54 ± 0.78
✓		✓		89.38 ± 0.75	91.51 ± 0.85
✓	✓	✓		90.51 ± 0.64	93.22 ± 0.63
✓	✓	✓	✓	92.78 ± 0.78	95.18 ± 0.68

ADMANI. Table 2 shows the mAP and Recall @ 0.5 results, where BRAIDet shows an mAP of 88.34 for the ratio 1/16, which is 6.5% larger than the second best method, Soft Teacher. For the ratio 1/2, the mAP improvement is still large at around 4.5%. Similarly, for the Recall @ 0.5, BRAIDet is around 7% better than Soft Teacher (the second best method) for the ratio 1/16, and when the ratio is 1/2, the improvement is around 4%. The results from the partially labelled protocol on CBIS-DDSM on Table 4 are similar to ADMANI. Indeed, our BRAIDet

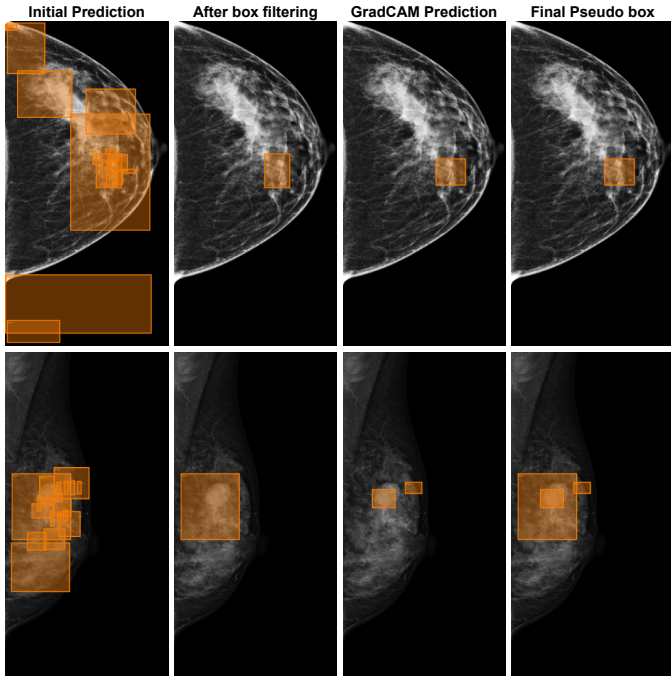


Fig. 6. Visualisation of the pseudo-labelling by the teacher using a CC (top) and an MLO (bottom) view of a weakly-annotated sample. The process starts with the initial predictions by the BRAIxDet teacher (first column), which is filtered to keep the detection with the highest score (second column). Next, we show the GradCAM detections produced by BRAIxMVCCL (Chen et al., 2022) (third column), and the final pseudo labels produced by the teacher to train the student with all GradCAM detections and the top BRAIxDet teacher detection (last column).

shows consistently better results than other approaches for all training ratios.

For instance, BRAIxDet presents an mAP of 53.99 for ratio 1/16, which is much larger than the second best, Unbiased Teacher, with a mAP of 36.18. For ratio 1/2, our mAP result is 5% better than Soft Teacher (second best). Similar conclusions can be drawn from the results of the Recall @ 0.5. Another interesting difference between the ADMANI and CBIS-DDSM results is the general lower performance on the CBIS-DDSM dataset. This can be explained by the lower quality of the images in the CBIS-DDSM dataset, as observed when comparing with Figures 7 and 8. It is worth noticing that in general, on both datasets, both BRAIxDet and competing SSL methods show better mAP and Recall @ 0.5 results than Faster RCNN, demonstrating the importance of using not only the fully-annotated cases, but also the weakly-annotated training subset.

The results produced by BRAIxDet and competing approaches using the fully labelled protocol on ADMANI using extra weakly-labelled data (the number of extra weakly labelled images are defined inside the brackets) are shown in Table 3. The mAP results confirm that BRAIxDet shows an improvement of 2.7% with respect to the second best approach Soft Teacher. Similarly, BRAIxDet’s Recall @ 0.5 results show an improvement of around 2.5% over competing SSL methods. Similarly to the partially labelled protocol from Table 2,

Table 7. Comparison of different types of batch normalisation (BN) strategies for the student-teacher SSL stage. The first row shows the mAP and Recall @ 0.5 results using the usual approach, where the student updates its own BN statistics, but the teacher does not update the BN statistics from pre-training. Second row shows the competing approach (Cai et al., 2021) that updates the teacher’s BN statistics with the EMA from the student’s BN statistics. The last row shows our proposed approach based on freezing both the student and teacher BN statistics. Results are computed using the fully-labelled protocol on ADMANI dataset (Frazer et al., 2022).

Methods	mAP	Recall @ 0.5
Open BN (Tarvainen and Valpola, 2017)	89.95 ± 0.52	92.71 ± 0.83
EMA BN (Cai et al., 2021)	90.44 ± 0.63	93.05 ± 0.59
Pre-estimated BN (ours)	92.78 ± 0.78	95.18 ± 0.68

BRAIxDet and competing SSL methods show better mAP and Recall @ 0.5 results than Faster RCNN. We also present the testing performance results of malignant breast lesion detection models on supervised subsets of ADMANI (Frazer et al., 2022) and DDSM (Smith, 2017), shown in Table 5 (without using any extra weakly labelled images). We show that our approach also outperforms the previous breast lesion detection methods in the context of classic supervised learning. We notice that there is a large gap between all models’ performance on ADMANI (Frazer et al., 2022) and DDSM (Smith, 2017). For example, the mAP results on ADMANI testing images when training on the 1/16 partition (430 images) is 5.18% better than the results on DDSM with 3/4 partition (780 images). The major reason for the discrepancy in performance is attributed to the data quality as the DDSM was completed in 1997, whereas the ADMANI dataset was collected between 2013 and 2019 and completed in 2021.

We performed a one-tailed t-test (between our BRAIxDet and the second best method) using the results from Tables 2, 4 and showed that we achieved p -values less than 0.05 for all partitions for both ADMANI and CBIS-DDSM datasets. In Table 3, we surpassed the second best method Soft Teacher (Xu et al., 2021) by 2.49% and 2.47% on the test set with p -values equal to 0.0007 and 0.0001, respectively for mAP and FROC measures. We conclude that our result is significantly better than previous methods for all experimental protocols. Moreover, the results in Fig. 2 and Fig. 4 reveal that for our BRAIxDet, a decrease in the amount of fully annotated data does not result in a significant decrease in model performance. This evidence indicates that our proposed method is more effective than other methods when applied to datasets with incomplete annotations at various levels of missing data.

We visualise the detection results by the most competitive methods and our proposed BRAIxDet model on ADMANI (Figure 7) and on CBIS-DDSM (Figure 8). In general, we can see that our method is more robust to false positive detections, while displaying more accurate true positive detections. We also show the cross-view detections on the CC and MLO mammograms from the same breast in Figure 9. Notice how BRAIxDet is robust to false positives, and at the same time precise at detecting the true positives from both views. We believe that such cross-view accuracy is enabled in part by the cross-view analysis provided by BRAIxDet.

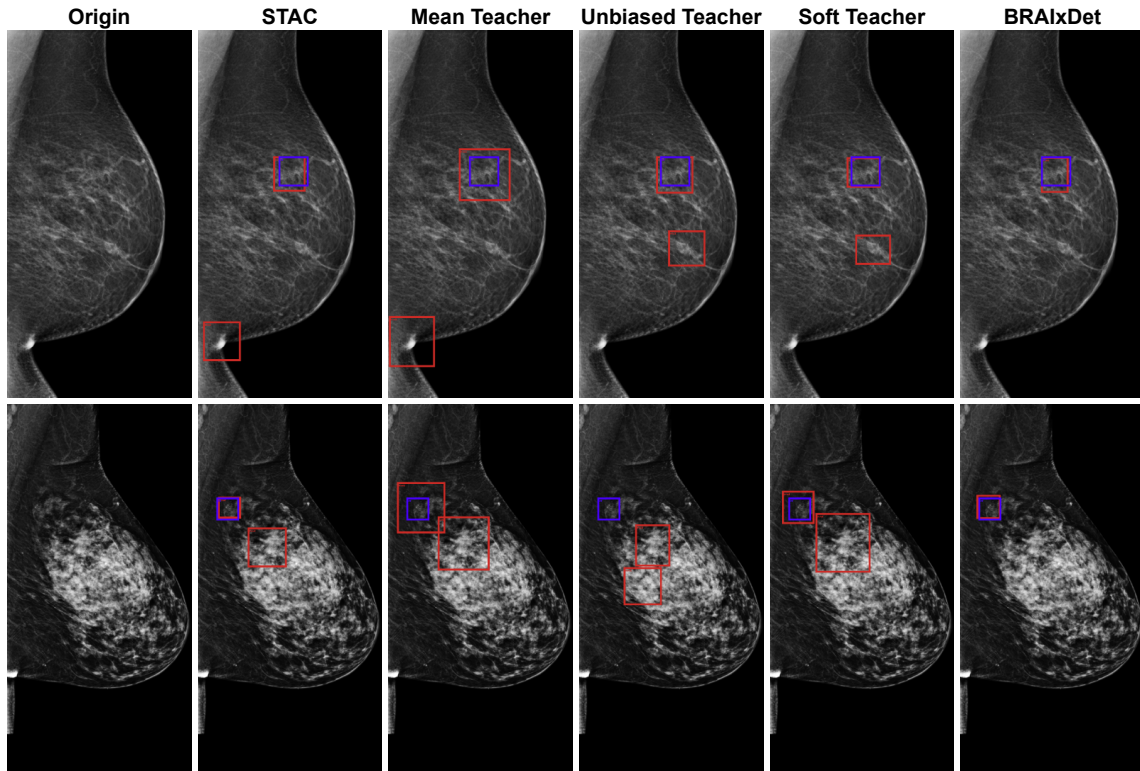


Fig. 7. Visualisation of the results achieved by the most competitive methods and our BRAIxDet (column titles show each method's name) on two ADMANI testing images, where the **blue** rectangles show lesion annotations and the **red** rectangles display the detections.

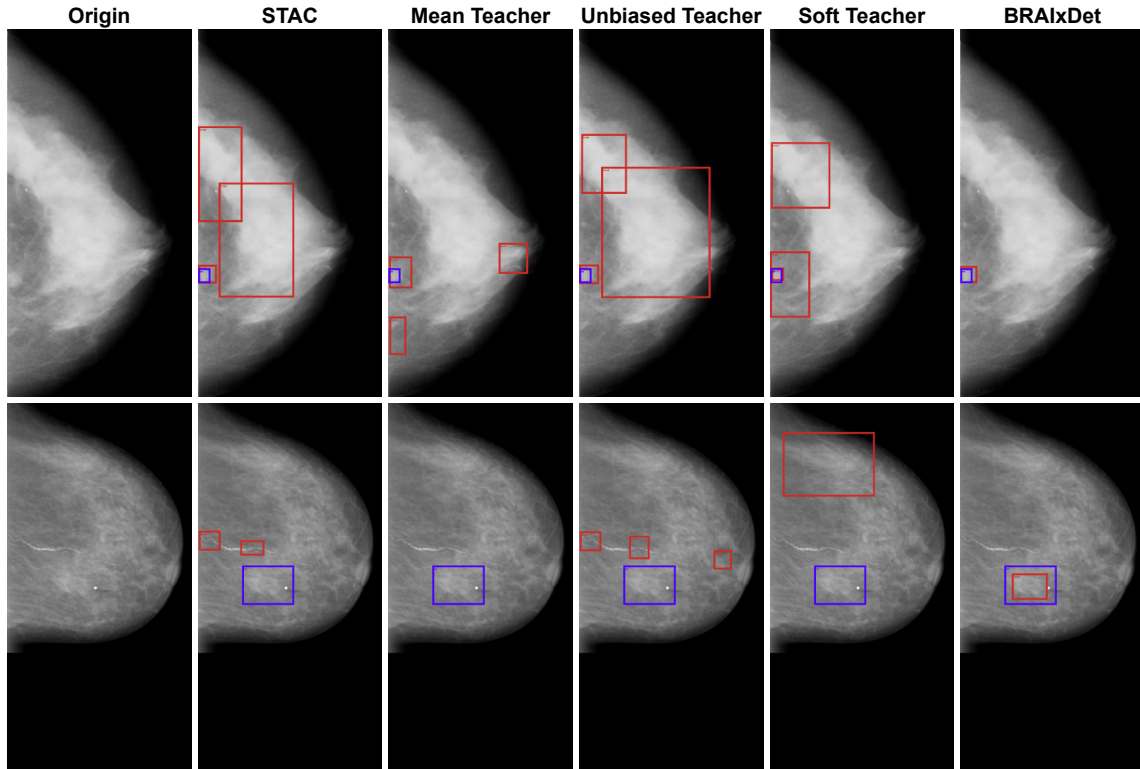


Fig. 8. Visualisation of the results achieved by the most competitive methods and our BRAIxDet (column titles show each method's name) on two CBIS-DDSM testing images, where the **blue** rectangles show the lesion annotations, and the **red** rectangles display the detections.

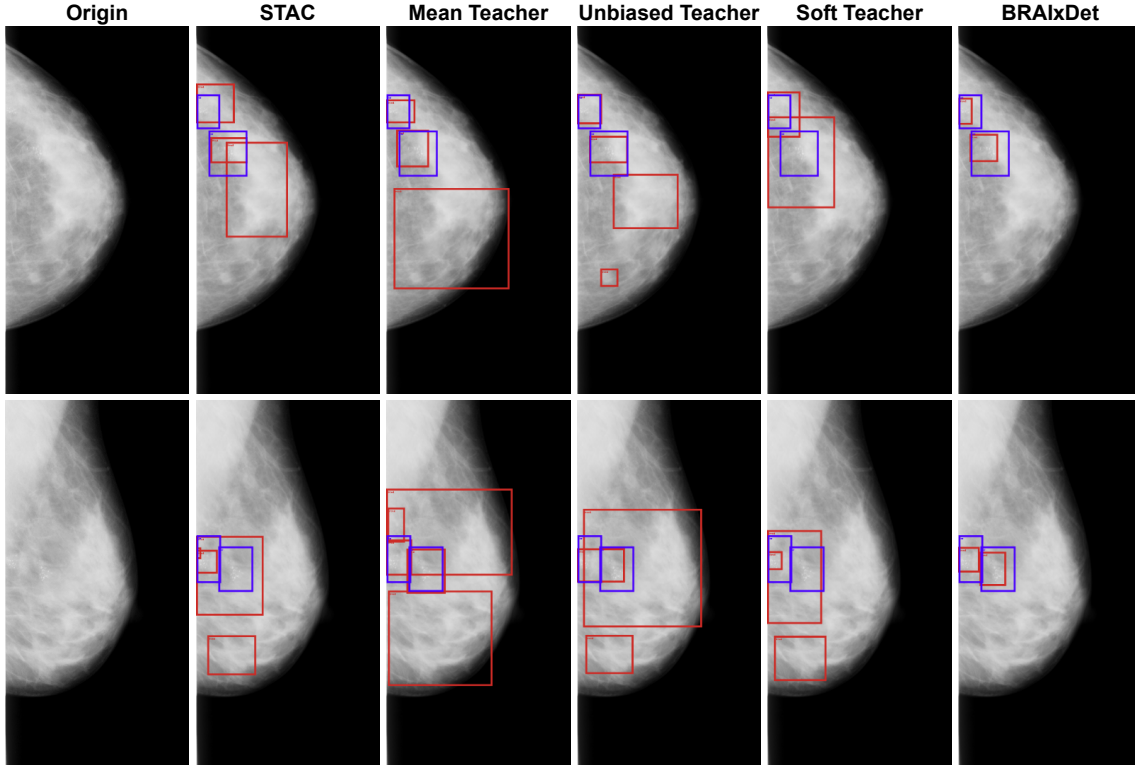


Fig. 9. Visualisation of the cross-view results achieved by several methods and our BRAIxDet (column titles show each method’s name) on CBIS-DDSM testing images containing two views of the same breast, where blue rectangles show lesion annotations and red rectangles display the detections. Note that BRAIxDet is the only method that correctly localises both lesions in the two views, showing the importance of the cross-view analysis.

4.5. Ablation study

In this ablation study, we first show a visual example of the steps in the production of a pseudo-label for weakly-annotated images by the teacher in Figure 6. The process starts with the initial prediction from the BRAIxDet teacher model, which tends to be inaccurate, particularly at the initial SSL training stages. This issue is addressed in part by keeping only the most confident detection, as shown in the column ‘After box filtering’. In addition, the BRAIxDet teacher’s detection inaccuracies are also dealt with GradCAM predictions produced by BRAIxMVCCL (Chen et al., 2022), which are used with the most confident detection to produce the final pseudo-labelled detections.

Table 6 shows the impact of initial prediction results from GradCAM, the local co-occurrence module (LCM) from BRAIxMVCCL, the student-teacher SSL training, and the use of BRAIxMVCCL’s GradCAM detections for the pseudo-labelling process. All methods in this table first pre-train their EfficientNet-b0 classification backbone with the fully- and weakly-annotated training subsets. The first row shows the original GradCAM results. The second row shows the Faster RCNN (Ren et al., 2015) that is trained using only the fully-annotated training subset. The third row displays a method that pre-trains the multi-view BRAIxMVCCL classifier (Chen et al., 2022) and keeps the LCM for training the Faster RCNN, which shows that the multi-view analysis from LCM provides substantial improvement to the original Faster RCNN. The fourth row displays that our proposed student-teacher SSL training

improves the original Faster RCNN results because such training allows the use of the fully- and weakly-annotated training subsets. When combining Faster RCNN, LCM, and the student-teacher SSL training (fifth row), the results are better than without SSL training or without LCM. Putting all BRAIxDet components together (sixth row), including BRAIxMVCCL’s GradCAM detections, enables us to reach the best mAP and Recall @ 0.5 results.

Another important point that was investigated is the role of the proposed BN approach, which is presented in Table 7. The results show that the proposed approach based on freezing both the student and teacher BN statistics is better than just updating the student’s BN statistics, or updating both the student and teacher’s BN statistics (Cai et al., 2021).

In Fig. 5, we provide further ablation studies on the hyper-parameters α for EMA decay, the threshold τ for binarising the GradCAM heatmap, and the weighting factor λ that controls the contribution of the weakly-supervised loss. In general, we note that increasing the smoothing factor α makes the EMA process more robust to inaccurate student weights, leading to improved performance, as shown in Fig. 5(a). Also, the study of τ in Fig. 5(b) shows that $\tau = 0.5$ exhibits a slight improvement over other threshold values. Regarding λ in Fig. 5(c), we notice that small values (e.g., $\lambda \in [0.1, 0.5]$) lead to better performance, so we set it at 0.25. We hypothesize that the predictions from the teacher model may exhibit instability, and thus assigning a smaller weight helps mitigate the impact of inaccurate gradient directions.

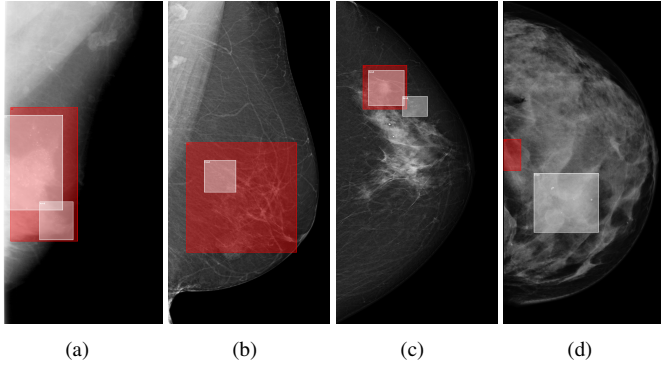


Fig. 10. Visualisations of four failure cases of BRAIxDet, where red boxes denote the manual labels, and white boxes represent the automatic detections from our system. The failure cases are the following: (a) multiple detected regions inside a large ground-truth annotation; (b) a small prediction within an excessively large annotation; (c) falsely detected benign region (i.e., false positive); and (d) miss-detected challenging malignant region (i.e., false positive and false negative).

4.6. Failure Cases

We show four failure cases produced by our system in Figure 10. We notice that CBIS-DDSM (Smith, 2017) and ADMANI (Frazer et al., 2022) often have overly large annotations, as shown in Fig. 10(a) and Fig. 10(b). Additionally, our findings reveal that the system faces challenges in distinguishing between benign and malignant lesions, particularly when it comes to benign calcification, as illustrated in Figure 10(c). This is due to the absence of benign annotations in the ADMANI dataset (Frazer et al., 2022). In addition, we observed that the current model is challenged by lesions represented by subtle changes compared to normal breast tissue, as shown in Figure 10(d), which we believe is a significant challenge for any automated mammogram lesion detection system.

4.7. Limitations.

A relevant limitation of our method is related to Grad-CAM, which is critical for the model, but can introduce some confirmation bias to the system as GradCAM only provides a coarse localization result that may include noisy labels. Also, localization methods like GradCAM will have difficulty identifying multiple overlapping objects as it is not designed to segment multiple independent instances. A limitation related to the annotations present in our datasets is that small lesions (e.g., micro-calcifications) can be detected as multiple bounding boxes, but the datasets ADMANI (Frazer et al., 2022) and CBIS-DDSM (Smith, 2017) tend to identify the areas that contain multiple micro-calcifications as a single instance. This discrepancy between the annotations and detections can lead to an artificial decrease in performance. A computational limitation is that the use of weakly annotated datasets motivate us to introduce an additional classification network, thereby introducing an increase in computational costs for the system. Another important limitation is that biases in the datasets (e.g., imaging manufacturers, population distribution) may impact our results.

5. Conclusion

In this paper, we proposed a new framework for training breast cancer lesion detectors from mammograms using real-world screening mammogram datasets. The proposed framework contains a new problem setting and a new method. The new setting is based on large-scale real-world screening mammogram datasets, which have a subset that is fully annotated and another subset that is weakly annotated with just the global image classification and without lesion localisation – we call this setting malignant breast lesion detection with incomplete annotations. Our solution to this setting is a new method with the following two stages: 1) pre-training a multi-view mammogram classifier with weak supervision from the whole dataset, and 2) extend the trained classifier to become a multi-view detector that is trained with semi-supervised student-teacher learning, where the training set contains fully and weakly-annotated mammograms. We provide extensive detection results on two real-world screening mammogram datasets containing fully and weakly annotated mammograms, which show that our proposed approach has SOTA results in the detection of malignant breast lesions with incomplete annotations. In the future, we aim to further improve model performance by incorporating additional multi-modal information (i.e., radiology reports, risk factors or ultrasound) to calibrate the confidence of the pseudo-label.

Acknowledgments

This work was supported by funding from the Australian Government under the Medical Research Future Fund - Grant MRFAI000090 for the Transforming Breast Cancer Screening with Artificial Intelligence (BRAIx) Project. G. Carneiro acknowledges the support by the Australian Research Council through grants DP180103232 and FT190100525.

References

- Agarwal, R., Diaz, O., Yap, M.H., Lladó, X., Marti, R., 2020. Deep learning for mass detection in full field digital mammograms. *Computers in biology and medicine* 121, 103774.
- Bar, Y., Diamant, I., Wolf, L., Lieberman, S., Konen, E., Greenspan, H., 2015. Chest pathology detection using deep learning with non-medical training. in: 2015 IEEE 12th international symposium on biomedical imaging (ISBI), IEEE. pp. 294–297.
- Brem, R.F., Baum, J., Lechner, M., Kaplan, S., Souders, S., Naul, L.G., Hoffmeister, J., 2003. Improvement in sensitivity of screening mammography with computer-aided detection: a multiinstitutional trial. *American Journal of Roentgenology* 181, 687–693.
- Butler, D., Zhang, Y., Chen, T., Shin, S.H., Singh, R., Carneiro, G., 2022. In defense of kalman filtering for polyp tracking from colonoscopy videos. in: 2022 IEEE 19th International Symposium on Biomedical Imaging (ISBI), IEEE. pp. 1–5.
- Cai, Z., Ravichandran, A., Maji, S., Fowlkes, C., Tu, Z., Soatto, S., 2021. Exponential moving average normalization for self-supervised and semi-supervised learning. in: Proceedings of the IEEE/CVF Conference on Computer Vision and Pattern Recognition, pp. 194–203.
- Carion, N., Massa, F., Synnaeve, G., Usunier, N., Kirillov, A., Zagoruyko, S., 2020. End-to-end object detection with transformers. in: European conference on computer vision, Springer. pp. 213–229.
- Carneiro, G., Nascimento, J., Bradley, A.P., 2017. Automated analysis of unregistered multi-view mammograms with deep learning. *IEEE transactions on medical imaging* 36, 2355–2365.

- Chen, C., Li, O., Tao, D., Barnett, A., Rudin, C., Su, J.K., 2019. This looks like that: deep learning for interpretable image recognition. *Advances in neural information processing systems* 32.
- Chen, Y., Wang, H., Chong, W., Tian, Y., Liu, F., Liu, Y., Elliott, M., Davis, M., Frazer, H., Carneiro, G., 2022. Multi-view local co-occurrence and global consistency learning improve mammogram classification generalisation, in: *International Conference on Medical Image Computing and Computer-Assisted Intervention*.
- Clancy, K., Aboutalib, S., Mohamed, A., Sumkin, J., Wu, S., 2020. Deep learning pre-training strategy for mammogram image classification: an evaluation study. *Journal of Digital Imaging* 33, 1257–1265.
- Dhungel, N., Carneiro, G., Bradley, A.P., 2015. Automated mass detection in mammograms using cascaded deep learning and random forests, in: *2015 international conference on digital image computing: techniques and applications (DICTA)*, IEEE. pp. 1–8.
- Dhungel, N., Carneiro, G., Bradley, A.P., 2017. A deep learning approach for the analysis of masses in mammograms with minimal user intervention. *Medical image analysis* 37, 114–128.
- Fenton, J.J., Abraham, L., Taplin, S.H., Geller, B.M., Carney, P.A., D’Orsi, C., Elmore, J.G., Barlow, W.E., Consortium, B.C.S., 2011. Effectiveness of computer-aided detection in community mammography practice. *Journal of the National Cancer institute* 103, 1152–1161.
- Fenton, J.J., Taplin, S.H., Carney, P.A., Abraham, L., Sickles, E.A., D’Orsi, C., Berns, E.A., Cutter, G., Hendrick, R.E., Barlow, W.E., et al., 2007. Influence of computer-aided detection on performance of screening mammography. *New England Journal of Medicine* 356, 1399–1409.
- Frazer, H.M., Tang, J.S., Elliott, M.S., Kunicki, K.M., Hill, B., Karthik, R., Kwok, C.F., Peña-Solorzano, C.A., Chen, Y., Wang, C., et al., 2022. Admani: Annotated digital mammograms and associated non-image datasets. *Radiology: Artificial Intelligence* 5, e220072.
- Girshick, R., 2015. Fast r-cnn, in: *Proceedings of the IEEE international conference on computer vision*, pp. 1440–1448.
- Hadjjiiski, L., Sahiner, B., Chan, H.P., 2006. Advances in cad for diagnosis of breast cancer. *Current opinion in obstetrics & gynecology* 18, 64.
- He, K., Zhang, X., Ren, S., Sun, J., 2016. Deep residual learning for image recognition, in: *Proceedings of the IEEE conference on computer vision and pattern recognition*, pp. 770–778.
- Hu, H., Gu, J., Zhang, Z., Dai, J., Wei, Y., 2018. Relation networks for object detection, in: *Proceedings of the IEEE conference on computer vision and pattern recognition*, pp. 3588–3597.
- Hupse, R., Karssemeijer, N., 2009. Use of normal tissue context in computer-aided detection of masses in mammograms. *IEEE Transactions on Medical Imaging* 28, 2033–2041.
- Hupse, R., Samulski, M., Lobbes, M., Den Heeten, A., Imhof-Tas, M.W., Beijerinck, D., Pijnappel, R., Boetes, C., Karssemeijer, N., 2013. Standalone computer-aided detection compared to radiologists’ performance for the detection of mammographic masses. *European radiology* 23, 93–100.
- Jeong, J., Lee, S., Kim, J., Kwak, N., 2019. Consistency-based semi-supervised learning for object detection. *Advances in neural information processing systems* 32.
- Kingma, D.P., Ba, J., 2014. Adam: A method for stochastic optimization. *arXiv preprint arXiv:1412.6980*.
- Laine, S., Aila, T., 2016. Temporal ensembling for semi-supervised learning. *arXiv preprint arXiv:1610.02242*.
- Lauby-Secretan, B., Scoccianti, C., Loomis, D., Benbrahim-Tallaa, L., Bouvard, V., Bianchini, F., Straif, K., 2015. Breast-cancer screening—viewpoint of the iarc working group. *New England journal of medicine* 372, 2353–2358.
- LeCun, Y., Bengio, Y., Hinton, G., 2015. Deep learning. *nature* 521, 436–444.
- Lee, R.S., Gimenez, F., Hoogi, A., Miyake, K.K., Gorovoy, M., Rubin, D.L., 2017. A curated mammography data set for use in computer-aided detection and diagnosis research. *Scientific data* 4, 1–9.
- Lehman, C.D., Wellman, R.D., Buist, D.S., Kerlikowske, K., Tosteson, A.N., Miglioretti, D.L., Consortium, B.C.S., et al., 2015. Diagnostic accuracy of digital screening mammography with and without computer-aided detection. *JAMA internal medicine* 175, 1828–1837.
- Lei, Y., Tian, Y., Shan, H., Zhang, J., Wang, G., Kalra, M.K., 2020. Shape and margin-aware lung nodule classification in low-dose ct images via soft activation mapping. *Medical image analysis* 60, 101628.
- Lin, T.Y., Goyal, P., Girshick, R., He, K., Dollár, P., 2017. Focal loss for dense object detection, in: *Proceedings of the IEEE international conference on computer vision*, pp. 2980–2988.
- Liu, L., Ouyang, W., Wang, X., Fieguth, P., Chen, J., Liu, X., Pietikäinen, M., 2020a. Deep learning for generic object detection: A survey. *International journal of computer vision* 128, 261–318.
- Liu, Y., Tian, Y., Chen, Y., Liu, F., Belagiannis, V., Carneiro, G., 2022. Perturbed and strict mean teachers for semi-supervised semantic segmentation, in: *Proceedings of the IEEE/CVF Conference on Computer Vision and Pattern Recognition*, pp. 4258–4267.
- Liu, Y., Zhang, F., Zhang, Q., Wang, S., Wang, Y., Yu, Y., 2020b. Cross-view correspondence reasoning based on bipartite graph convolutional network for mammogram mass detection, in: *Proceedings of the IEEE/CVF Conference on Computer Vision and Pattern Recognition*, pp. 3812–3822.
- Liu, Y., Zhou, Z., Zhang, S., Luo, L., Zhang, Q., Zhang, F., Li, X., Wang, Y., Yu, Y., 2019. From unilateral to bilateral learning: Detecting mammogram masses with contrasted bilateral network, in: *Medical Image Computing and Computer Assisted Intervention—MICCAI 2019: 22nd International Conference, Shenzhen, China, October 13–17, 2019, Proceedings, Part VI* 22, Springer. pp. 477–485.
- Liu, Y.C., Ma, C.Y., He, Z., Kuo, C.W., Chen, K., Zhang, P., Wu, B., Kira, Z., Vajda, P., 2021. Unbiased teacher for semi-supervised object detection. *arXiv preprint arXiv:2102.09480*.
- Ma, J., Li, X., Li, H., Wang, R., Menze, B., Zheng, W.S., 2021. Cross-view relation networks for mammogram mass detection, in: *2020 25th International Conference on Pattern Recognition (ICPR)*, IEEE. pp. 8632–8638.
- Oquab, M., Bottou, L., Laptev, I., Sivic, J., 2015. Is object localization for free?-weakly-supervised learning with convolutional neural networks, in: *Proceedings of the IEEE conference on computer vision and pattern recognition*, pp. 685–694.
- Paszke, A., Gross, S., Massa, F., Lerer, A., Bradbury, J., Chanan, G., Killeen, T., Lin, Z., Gimelshein, N., Antiga, L., et al., 2019. Pytorch: An imperative style, high-performance deep learning library. *Advances in neural information processing systems* 32, 8026–8037.
- Raghu, M., Zhang, C., Kleinberg, J., Bengio, S., 2019. Transfusion: Understanding transfer learning for medical imaging. *Advances in neural information processing systems* 32.
- Rajpurkar, P., Irvin, J., Zhu, K., Yang, B., Mehta, H., Duan, T., Ding, D., Bagul, A., Langlotz, C., Shpanskaya, K., et al., 2017. CheXnet: Radiologist-level pneumonia detection on chest x-rays with deep learning. *arXiv preprint arXiv:1711.05225*.
- Redmon, J., Divvala, S., Girshick, R., Farhadi, A., 2016. You only look once: Unified, real-time object detection, in: *Proceedings of the IEEE conference on computer vision and pattern recognition*, pp. 779–788.
- Ren, S., He, K., Girshick, R., Sun, J., 2015. Faster r-cnn: Towards real-time object detection with region proposal networks. *Advances in neural information processing systems* 28.
- Ribli, D., Horváth, A., Unger, Z., Pollner, P., Csabai, I., 2018. Detecting and classifying lesions in mammograms with deep learning. *Scientific reports* 8, 1–7.
- Russakovsky, O., Deng, J., Su, H., Krause, J., Satheesh, S., Ma, S., Huang, Z., Karpathy, A., Khosla, A., Bernstein, M., et al., 2015. Imagenet large scale visual recognition challenge. *International journal of computer vision* 115, 211–252.
- Seibold, C., Kleesiek, J., Schlemmer, H.P., Stiefelwagen, R., 2020. Self-guided multiple instance learning for weakly supervised disease classification and localization in chest radiographs, in: *Asian Conference on Computer Vision*, Springer. pp. 617–634.
- Selvaraju, R.R., Cogswell, M., Das, A., Vedantam, R., Parikh, D., Batra, D., 2017. Grad-cam: Visual explanations from deep networks via gradient-based localization, in: *Proceedings of the IEEE international conference on computer vision*, pp. 618–626.
- Selvi, R., 2014. *Breast diseases: imaging and clinical management*. Springer.
- Shen, L., Margolies, L.R., Rothstein, J.H., Fluder, E., McBride, R., Sieh, W., 2019a. Deep learning to improve breast cancer detection on screening mammography. *Scientific reports* 9, 1–12.
- Shen, Y., Wu, N., Phang, J., Park, J., Kim, G., Moy, L., Cho, K., Geras, K.J., 2019b. Globally-aware multiple instance classifier for breast cancer screening, in: *International Workshop on Machine Learning in Medical Imaging*, Springer. pp. 18–26.
- Shen, Y., Wu, N., Phang, J., Park, J., Liu, K., Tyagi, S., Heacock, L., Kim, S.G., Moy, L., Cho, K., et al., 2021. An interpretable classifier for high-resolution breast cancer screening images utilizing weakly supervised localization. *Medical image analysis* 68, 101908.
- Smith, K., 2017. Cbis-ddsm. <https://wiki.cancerimagingarchive>.

- [net/display/Public/CBIS-DDSM](#). [Online; accessed 21-August-2021].
- Sohn, K., Zhang, Z., Li, C.L., Zhang, H., Lee, C.Y., Pfister, T., 2020. A simple semi-supervised learning framework for object detection. arXiv preprint arXiv:2005.04757 .
- Sung, H., Ferlay, J., Siegel, R.L., Laversanne, M., Soerjomataram, I., Jemal, A., Bray, F., 2021. Global cancer statistics 2020: Globocan estimates of incidence and mortality worldwide for 36 cancers in 185 countries. *CA: a cancer journal for clinicians* 71, 209–249.
- Tan, M., Le, Q., 2019. Efficientnet: Rethinking model scaling for convolutional neural networks, in: International Conference on Machine Learning, PMLR. pp. 6105–6114.
- Tarvainen, A., Valpola, H., 2017. Mean teachers are better role models: Weight-averaged consistency targets improve semi-supervised deep learning results. *Advances in neural information processing systems* 30.
- Vu, Y.N.T., Tsue, T., Su, J., Singh, S., 2021. An improved mammography malignancy model with self-supervised learning, in: *Medical Imaging 2021: Computer-Aided Diagnosis*, SPIE. pp. 210–216.
- Wang, X., Peng, Y., Lu, L., Lu, Z., Bagheri, M., Summers, R.M., 2017. Chestx-ray8: Hospital-scale chest x-ray database and benchmarks on weakly-supervised classification and localization of common thorax diseases, in: *Proceedings of the IEEE conference on computer vision and pattern recognition*, pp. 2097–2106.
- Xu, M., Zhang, Z., Hu, H., Wang, J., Wang, L., Wei, F., Bai, X., Liu, Z., 2021. End-to-end semi-supervised object detection with soft teacher, in: *Proceedings of the IEEE/CVF International Conference on Computer Vision*, pp. 3060–3069.
- Yang, Z., Cao, Z., Zhang, Y., Han, M., Xiao, J., Huang, L., Wu, S., Ma, J., Chang, P., 2020. Momminet: Mammographic multi-view mass identification networks, in: *International Conference on Medical Image Computing and Computer-Assisted Intervention*.
- Yang, Z., Cao, Z., Zhang, Y., Tang, Y., Lin, X., Ouyang, R., Wu, M., Han, M., Xiao, J., Huang, L., et al., 2021. Momminet-v2: Mammographic multi-view mass identification networks. *Medical Image Analysis* , 102204.
- Yao, L., Prosky, J., Poblenz, E., Covington, B., Lyman, K., 2018. Weakly supervised medical diagnosis and localization from multiple resolutions. arXiv preprint arXiv:1803.07703 .
- Zhou, B., Khosla, A., Lapedriza, A., Oliva, A., Torralba, A., 2016. Learning deep features for discriminative localization, in: *Proceedings of the IEEE conference on computer vision and pattern recognition*, pp. 2921–2929.